Facultad de ciencias

Influence of vibronic coupling over the geometry and magnetism of layered perovskites and silver difluoride

Influencia del acoplamiento vibrónico sobre la geometría y magnetismo de perovskitas en capas y difloruro de plata

Trabajo de Fin de Máster
para acceder al título de

MÁSTER INTERUNIVERSITARIO EN QUÍMICA TEÓRICA Y MODELIZACIÓN COMPUTACIONAL

Autor: Inés Sánchez de Movellán Sáiz

Director: José Antonio Aramburu-Zabala Higuera

Julio - 2021

Al que para mí es un hermano, Fernando

Agradecimientos

En primer lugar, quiero expresar mi agradecimiento al grupo de Física Teórica de la Materia Condensada, que me ha acogido como una más, me ha formado durante estos últimos años y me ha apoyado en los momentos más complicados. En particular, quiero mencionar a mi director, Antonio Aramburu-Zabala, que durante los últimos años del grado despertó mi interés por la física de los sólidos, interés que desde entonces no ha dejado de aumentar. Gracias también a Pablo García, Miguel Moreno y Javier Junquera, por permitirme aprender de vosotros y transmitirme vuestra pasión por esta materia.

Quiero mencionar aquí a Laura y a Carmen, que han sentido mi ilusión con este trabajo tanto como yo, y viven mis victorias y derrotas como si fueran suyas. A Alba, Carla, César y mis demás compañerines por vuestro apoyo y vuestra amistad, y por supuesto a mi familia, en especial a mi madre, a Fernando y a Silvia, que siempre han estado y siempre estarán conmigo.

Por último, no me puedo olvidar de mis compañeros condensados, Toraya, Nayara, Fer y Raúl, con los que he pasado mi día a día durante este tiempo, compartiendo dudas, frustraciones, enfados con la física, risas y alguna que otra lloradita. También a los fotónicos, con los que espero seguir compartiendo campo de estudio, facultad y jueves de CDs. A Lavín, mi futuro meteorólogo favorito, capaz de sacarme una sonrisa hasta en los días más duros y a Pablo, que, aunque lleva cinco minutos en mi vida, me ha dado todo su apoyo, ayudándome a hacer las paces con este trabajo en muchos momentos.

¡Muchas gracias!

Abstract

The current interest in layered systems is encouraged by the discovery of a broad range of new properties and effects, such as superconducting states, 2D magnetism or insulator-metal transitions. High-temperature superconductors are characterized by two main features, namely, layered structure and antiferromagnetic coupling. Along this line, it has been proposed that a possible superconducting state could be observed in silver difluoride AgF_2 as a result of its apparent layered structure and strong intraplanar antiferromagnetism. Nevertheless, the buckling of the layers seems to prevent this transition to the superconducting state. On the other hand, the two mentioned properties of superconductors can be found in La_2CuO_4, that belongs to the Ruddlesden-Popper phase of layered perovskites, in which Heisenberg ferromagnets K_2CuF_4 and Cs_2AgF_4 are also included.

As a common aspect, in the four systems there is a strong dependence on the magnetic order with their structural distortions, which are induced by the electron-phonon coupling (the so-called vibronic coupling in the literature). However, the low symmetry of these compounds suggests that the usual interpretation within Jahn-Teller effect models requires further analysis. Therefore, we have studied them from a different perspective, focusing on the symmetry of the parent phases and their distortions to the experimentally measured structures. In addition, magnetic order has been considered in both parent and experimental phases as well as throughout the distortion.

To this end, first-principles periodic simulations have been carried out using Crystal software, which allows performing calculations of electronic structure on solids. In order to provide insight on the band structure of layered perovskites, a first-principles-based (second-principles) model has been used. Additionally, we have perform cluster calculations with Amsterdam density functional code, employed to simulate transition-metal complexes. Based on the results of these calculations, we have observed that the magnetic order of AgF_2 depends on the cooperative distortion of AgF_6^{4-} complexes and lattice parameters, whereas the calculations in layered perovskites K_2CuF_4 and Cs_2AgF_4 indicate that the covalent contribution, coming from the vibronic coupling with excited states, seems to be the main cause of the change in the magnetism. As a salient feature, we have observed that the three fluoride systems present ferroelasticity, a property strongly related with magnetism in these systems.

Keywords: vibronic coupling, magnetism, symmetry, first-principles simulations, layered perovkistes, ferroelasticity.

Resumen

El interés actual en los sistemas en capas viene motivado por el descubrimiento de un amplio abanico de nuevas propiedades y efectos, como transiciones a estados superconductores, magnetismo en 2D o transiciones metal-aislante. Los superconductores de alta temperatura tienen dos características principales: estructura en capas y acoplamiento antiferromagnético en la capa. En esta línea, se ha propuesto que un estado superconductor podría ser observado en el difuoruro de plata AgF_2, como resultado de su aparente estructura en capas y fuerte antiferromagnetismo dentro de la capa. Sin embargo, la deformación de las capas parece impedir la transición a la fase superconductora. Por otra parte, las dos propiedades mencionadas están presentes en La_2CuO_4, que pertenece a la fase Ruddlesden-Popper dentro de las perovskitas en capas, entre las que se incluyen también los ferromagnéticos de Heisenberg K_2CuF_4 y Cs_2AgF_4.

Una característica común a los cuatro sistemas es la fuerte dependencia entre el orden magnético y las distorsiones estructurales inducidas por el acoplamiento entre electrones y núcleos (el llamado acoplamiento vibrónico en la literatura). Sin embargo, la baja simetría de estos compuestos sugiere que la interpretación habitual dentro de los modelos de efecto Jahn-Teller requiere un análisis más detallado. Por tanto, en este trabajo hemos tomado una perspectiva diferente, centrándonos en la simetría de la fases madre y en sus distorsiones hasta las estructuras observadas experimentalmente. Además, se ha considerado el orden magnético tanto en las fases madre y experimental como a lo largo de la distorsión.

Con este objetivo, se han realizado simulaciones de primeros principios en sistemas periódicos mediante el programa Crystal, que permite hacer cálculos de estructura electrónica en sólidos. Para interpretar la estructura de bandas de las perovskitas en capas se ha usado un modelo basado en primeros principios (segundos principios). Complementariamente, se han llevado a cabo cálculos en agrupaciones de átomos con el código Amsterdan density functional, usado para simular complejos de metales de transición. A partir de los resultados obtenidos, se ha observado que el orden mágnetico del AgF_2 depende de la distorsión cooperativa de los complejos AgF_6^{4-} y de los parámetros de red, mientras que los cálculos en K_2CuF_4 y Cs_2AgF_4 apuntan a que la contribución debida a la covalencia que proviene del acoplamiento vibrónico con estados excitados es la principal causa de los cambios en el magnetismo. Un rasgo destacado en estos sistemas es que presentan ferroelasticidad, una propiedad fuertemente relacionada con el magnetismo en estos casos.

Palabras clave: acoplamiento vibrónico, magnetismo, simetría, simulaciones de primeros principios, perovskitas en capas, ferroelasticidad.

Contents

1. Introduction

Since the discovery of superconductor oxocuprates in 1986 [1], a great deal of interest has been paid to layered superconductors, due to the emergence of non-BCS and high-temperature (high-T_C) superconductivity. During the last three decades, new types of superconductors with unusual mechanisms and properties have been studied. Intense research efforts have been focused on developing new transition-metal based high-T_C superconductors. Among other examples, in 2008 the discovery of the iron-based layered superconductor $La[O_{1-x}F_x]FeAs$ was reported. This system experiences a superconducting transition when doped with F^- ions occupying O^{2-} atomic sites [2].

Currently, the field of layered superconductors is still developing. Despite improvements in the understanding of the nature of superconducting state in layered systems in recent years, unresolved issues remain, partly due to the strong electron correlation and competition between various effects, leading to different phases fairly close in energy [3]. Furthermore, in layered materials, which are highly two-dimensional systems, the strong intralayer coupling and weak interlayer interaction originate new electronic and magnetic states. Their quantum states along with the ability to change their properties by modifying composition or size have turned layered materials a relevant topic in solid state physics.

In the search for new high-T_C superconductors, it has been proposed that superconductivity could be observed in doped Ag^{2+} flourides [4], due to their apparent similarities with layered cuprate La_2CuO_4, such as the strong antiferromagnetic (AFM) coupling in the layer and the electronic configuration, since both compounds contain d^9 transition-metal ions. Seemingly, this possible superconducting state is frustrated by the buckling of the atomic layers (see Figure 1.1).

Understanding the properties of layered solids is a crucial point in order to achieve their full potential. Then, the first step is to analyse their crystalline structure at normal conditions. However, unraveling the microscopic origin of each structure is complicated due to the large number of interactions and instabilities that give rise to different structures whose energies can be very close.

Bearing all these facts in mind, in this work four layered systems have been studied, namely, the layered perovskites K_2CuF_4, Cs_2AgF_4 and La_2CuO_4 and the silver difluoride AgF_2. They contain the transition-metal complexes CuF_6^{4-}, AgF_6^{4-} and CuO_6^{8-}, where the central cation M (M = Cu^{2+}, Ag^{2+}) is sixfold coordinated by the anions (F^-, O^{2-}), henceforth called ligands. The electronic configuration of the central cation is d^9 ($3d^9$ in Cu^{2+}, $4d^9$ in Ag^{2+}). This open shell configuration involves a non-symmetric electron density in the transition-metal ion which causes a net force over ligands, that induces structural distortions which have been largely associated with Jahn-Teller (JT) effect [4] - [9], where the initial local symmetry of the complexes is octahedral. This usual interpretation has lead to misleading conclusions about distortions and magnetism. In this work we have followed a different path, focusing mainly on the symmetry of the systems, instead of using rough JT models.

As we will see in Section 3, the JT effect is a particular case of electron-phonon (vibronic) coupling, in which tight conditions of symmetry and electronic degeneration must be fulfilled. However, the low-symmetry (orthorhombic) of these compounds indicates that further analysis is required. Vibronic interactions present in these systems are ac-

compained by a spontaneous symmetry breaking, one of the most active topics in current research in the field of physics. One of the key elements in vibronic coupling problems is the concept of *parent phase* from which the experimental phase comes, and whose analysis has been a crucial point in this work. From first-principles simulations, we are able to calculate the ground state of this parent phase and, therefore, the structural distortion to the experimentally observed structure can be studied.

In this project we are especially focused on the relation between crystalline structure and magnetism. Specifically, we have analysed how the distortion due to vibronic coupling affects the magnetic order of the ground state, with the ultimate goal of controlling magnetic order by changing the structure of the system. It can be remarked the importance of parent phase analysis carried out in this work, in terms of both crystalline and magnetic structures, and their underlying relation. This analysis has been performed by means of first-principles simulations in the framework of spin-unrestricted Kohn-Sham density functional theory (KS-DFT). First-principles calculations are a powerful tool for understanding experimental results, analysing properties and phenomena that cannot be studied experimentally, such as non-equilibrium phases or metastable states, as well as in the design of new materials. In addition, a simple model of second-principles simulations have been used in order to obtain a first approximation of the band structure of layered perovskites, and its relation with magnetism.

1.1. Objectives and structure of this work

As mentioned above, the main purpose of this work is to inquire the consequences of vibronic coupling over crystalline and magnetic structures of four systems containing MX_6 complexes ($M = Ag^{2+}$, Cu^{2+}, $X = F^-$, O^{2-}): fluoroargentate AgF_2 and layered perovskites K_2CuF_4, Cs_2AgF_4 and La_2CuO_4. Accordingly, this work is divided in two parts. The first is dedicated to AgF_2 while the second concerns the three layered systems, as explained below:

- First, we have studied the structure of AgF_2 as well as the ground state of AgF_6^{4-} complexes by means of DFT simulations. It is worth noting the importance of the analysis of the parent phase and the distortion, conducted by cooperative JT effect, from the parent high-symmetry phase to the experimental one. Furthermore, we have explored the apparent layered structure and the relation between magnetism and cooperative JT effect in this material, where we have found that the magnetic order is a direct consequence of vibronic coupling.

- Then, we have explored the geometry and magnetism of actual layered structures, K_2CuF_4, Cs_2AgF_4 and La_2CuO_4. In the first two materials we have found a change in the magnetic order from AFM in the high-symmetry parent phase to ferromagnetic (FM) in the low-symmetry phase, when the systems are distorted following an orthorhombic distortion caused by pseudo Jahn-Teller (PJT) effect. By contrast La_2CuO_4 is stable under the same deformation.

This work is organized as follows: in the next two parts (Sections 1.2 and 1.3) fluoroargentate and layered perovskites are introduced. Then, in Section 2, the computational methods employed and their fundamentals are described, as well as the details of our calculations. Section 3 is dedicated to vibronic coupling and its associated effects (JT and PJT effects), including its relation with magnetic order. The next two parts, Section 4

and Section 5 cover the results and analysis of the computational study of AgF_2 and layered perovskites respectively, as well as the comparation between them. Finally, Section 6 collects the main conclusions of this work and future research in this area.

1.2. AgF_2

Among high-T_C superconducting materials, cuprate superconductors are a family of systems composed by layers of copper oxides CuO_2 alternating with layers of other metal oxides. Superconductivity comes from the strongly interacting d^9 electrons in the mentioned CuO_2 slabs. In these materials, the ground state of the so-called parent phase is found to be an antiferromagnetically ordered Mott insulator [10], in which the different chemical structure of the layers helps localizing the electrons in the layer and preventing the electron hopping between them.

Although the mechanism by which high-T_C superconductivity in cuprates occurs is still under debate, there are some shared properties present in this effect, such as the previously mentioned layered structure and AFM ground state. In addition, it can be noted the presence of elongated CuO_6 complexes, usually related to the JT effect.

During the last years, the search of d^9 superconductors has also turned to compounds containing $4d^9$ Ag^{2+} cations. As previously mentioned, it has been proposed that high-T_C superconductivity may be observed in doped Ag^{2+} flourides [4] [11], due to its apparent layered crystal structure and a charge transfer insulating ground state with strong AFM interaction within the layers [12]. Among Ag^{2+} fluorides we have been focused on the fluoroargentate AgF_2, whose structure is represented in Figure 1.1.

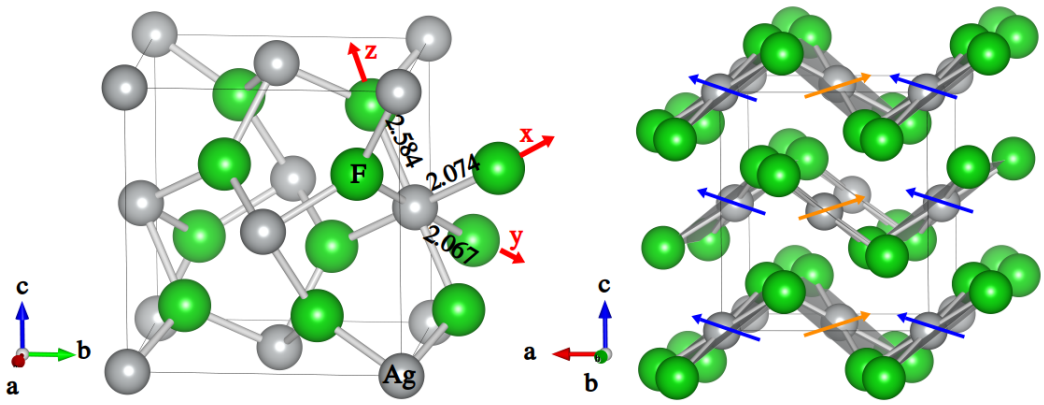

Figure 1.1: Left: orthorhombic Pbca structure of AgF_2. The complex AgF_6^{4-} and Ag^{2+}-F^- distances (in Å) are also represented. Right: layered structure of buckled AgF_2 sheets, including the non-collinear arrangement of spins (blue and orange arrows).

In this system, flourine opens the electronic d^{10} shell of silver. In contrast to Ag^+, for which there are more than 16000 known compounds, there are only about 100 systems containing Ag^{2+} cations [4]. The scarcity arises in the stability of Ag^{2+}, which tends to separate in Ag^+ and Ag^{3+}. Therefore, AgF_2 was not synthesised until 1971 by Fisher and coworkers [13]. For Ag^{2+} compounds, the presence of a more contracted 4d shell leads to an increase in covalency of the chemical bonding [4].

Regarding the formation of AgF_2 in the ionic picture, there is a transfer of hole from p-type orbitals of F to d-type orbitals of Ag and thus, AgF_2 is a charge transfer insulator, where electrons in 4d shell are strongly correlated.

As mentioned above, it has been proposed that electronic structure of AgF_2 is rather similar to insulating cuprates. However, it is more electronegative which complicates the doping. On the other hand, the buckling of AgF_2 planes, prevents the superexchange constant J from reaching values found for oxocuprates and enhaces self-trapping lattice effects (polarons) [12]. As shown in Figure 1.1, AFM order in **ab** plane of AgF_2 is characterized by a non-collinear arrangement of spins, which are tilted due to spin-orbit coupling (Dzyaloshinsky-Moriya interaction) [13]. Weak FM interaction is found in **bc** plane.

Recent studies based on first-principles calculations proposed that van der Waals forces are responsible of interlayer interaction, as occurs in graphite and thus, layers in AgF_2 should be easily exfoliable [14]. However, this conclusion seems contradictory with the apparently 3D structure of AgF_2 and the strong covalency of the Ag^{2+}-F^- bonds. Following these lines, in Section 4 we will discuss the origin of crystal structure of AgF_2 and its influence in the magnetism.

To this end, the analysis is divided in four main steps: (1) Exploration of the parent phase of AgF_2 and determination of its ground state (Section 4.1). (2) Analysis of the trigonal distortion from this reference phase (Section 4.2). (3) Study of cooperative effects and their connection with magnetism (Section 4.3). (4) Examination of the apparent layered structure of this compound as well as the presence of ferroelasticity (Section 4.4).

1.3. K_2CuF_4, Cs_2AgF_4 and La_2CuO_4

Over the last decades, a great deal of attention is focused on materials with perovskite-type structure. This family of structures comprise a wide range of systems with a huge amount of worthwhile properties at both fundamental and applied level. Among these properties, it can be noted the giant magnetorresistance in some manganites of $AMnO_3$ type, superconductivity in cuprates which stem from $ACuO_3$, Mott insulator-metal transitions and so on [15]. On the other hand, perovskites have played an important role in applications of different fields, such as spintronics and optoelectronics and recently, also in renewable energies sector, where new solar cells are based on hybrid inorganic-organic perovskites [16].

The basic perovskite structure is cubic with chemical formula ABX_3 [17], where A is usually a large cation (alkaline or rare earth elements), B a small cation (generally a transition-metal 3d, 4d or 5d) and X an anion (O^{2-}, F^-, Cl^-...). The tridimensional lattice is composed of BX_6 octahedrons that share corners, as shown in Figure 1.2 (b)

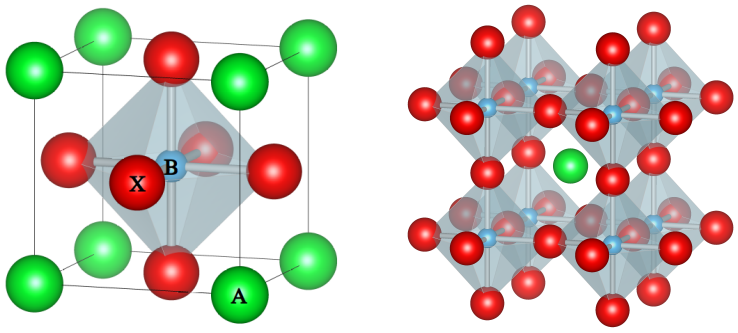

(a) (b)

Figure 1.2: (a) ABX_3 perovskite unit cell and (b) periodic structure

The chemical composition and structure of these systems together with the presence of d orbitals partially occupied, which usually involves strong electronic correlation and localization, lead to structural distortions (rotations and deformation of octahedrons, polar displacements) as well as the coexistence of different interactions [15].

Cubic perovskite is the basic structure for more complex systems, as the well-known layered perovskites, which are formed by 2D slabs of BX_6 units separated by some motif. Among the different types of layered perovskites, we have been focused on Ruddlesden-Popper phases A_2BX_4, where the slabs of sixfold coordinated complexes are alternated with layers of rock salt structure AX. In particular, our study is centred on K_2CuF_4, Cs_2AgF_4 and La_2CuO_4, whose conventional cells are represented in Figure 1.3.

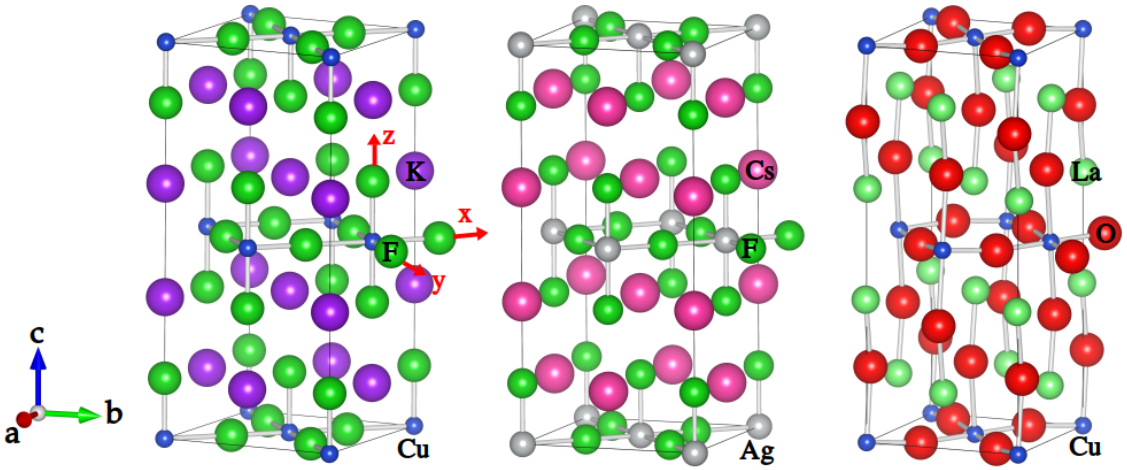

Figure 1.3: Layered perovskites K_2CuF_4 (left), Cs_2AgF_4 (center) and La_2CuO_4 (right) in the low symmetry (experimental) Cmca phase, including CuF_6^{4-}, AgF_6^{4-} and CuO_6^{8-} complexes.

In layered perovskites, small variations in the chemical composition may change significantly the geometry, symmetry, bonding and band structure, leading to a wide range of new 2D properties [15]. As in cubic perovskites, in these layered systems there are cooperative distortions and many physical interactions, which produce complex states. Consequently, understanding and modelling this sort of compounds is quite complicated and requires physical insight of its structure and properties.

Among these systems, K_2CuF_4 and Cs_2AgF_4 are Heisenberg ferromagnets, i.e., they show FM order in the plane orthogonal to c axis. The FM phenomena of transition-metal pairs in crystals and molecules have been an extensively interesting problem for physicists, chemists and biochemists. In order to describe the FM properties, several physical models have been proposed [18].

The three compounds comes from the parent structure K_2NiF_4, which belongs to the tetragonal space group I4/mmm (see Figure 5.1). These systems undergo a distortion from the high-symmetry phase to the low-symmetry orthorhombic phase Cmca, which has significant implications in the magnetic order displayed by them. It is worth noting the key role of orbital degree of freedom in order to understand both crystalline and magnetic structure of these systems [19].

Despite the three layered perovskites comes from the same parent structure and their electronic configuration is quite similar (d^9) they show different behaviour. K_2CuF_4 and

Cs_2AgF_4 present antiferrodistortive (AFD) orbital order and are FM in **ab** plane [19]. By contrast, La_2CuO_4 shows strong AFM coupling, and the orbital ordering is ferrodistortive (FD). The terminology of FD and AFD follows the classification proposed by Kanamori [20]. In insulating solids with open shell ions involving degenerate electronic states, vibronic coupling, which leads to JT distortions between adyacent atoms (see Section 3), produces long-range structural order [19]. Kanamori classified these distortions in FD when all sites in the lattice are aligned and AFD where the distortions are opposite in neighboring sites (see Figure 1.4).

Following these lines, Kugel and Khomskii (KK) made a fundamental contribution to this field, showing that superexchange interaction in orbitally degenerate ions leads to cooperative orbital ordering. The cooperative distortion is a direct consequence of these orbital orderings [21]. In this model Kugel and Khomskii proposed that the exchange interaction, which is crucial to understand the magnetic order, may also affects the structure, contributing to crystal distortions.

Despite the success of KK model in predicting the AFD distortion and AFM order in cubic perovskites as $KCuF_3$, $KCrF_3$ or $LaMnO_3$, it fails when is applied to the high-symmetry parent phase of K_2CuF_4 and Cs_2AgF_4, where the correct ground state and orbital ordering is reached after considering the charge-transfer in the insulating state [22]. On the other hand, KK model does not explain why La_2CuO_4 shows different orbital and magnetic orderings.

In contrast to this short-range model, the strong difference in the orbital ordering of these compounds lies in the long-range electric field created by the lattice over the transition-metal complexes [19]. Althoug the high-symmetry parent phase is the same in all cases, in K_2CuF_4 the electrostatic potential stabilizes the equatorial component of CuF_6^4 units and, therefore, the electron is localized in $x^2 - y^2$, and the compound displays FD($3z^2 - r^2$) ordering. On the other hand, in La_2CuO_4 the axial component is lower in energy, favoring the electron localization in $3z^2 - r^2$ and FD($x^2 - y^2$) orbital ordering. The energy gap between $3z^2 - r^2$ and $x^2 - y^2$ when the electrostatic potential is taken into account ($\sim 0.3 - 0.4$ eV) is larger than the typical values of energies involved in JT effect or superexchange (typically lower than 0.1 eV) [19].

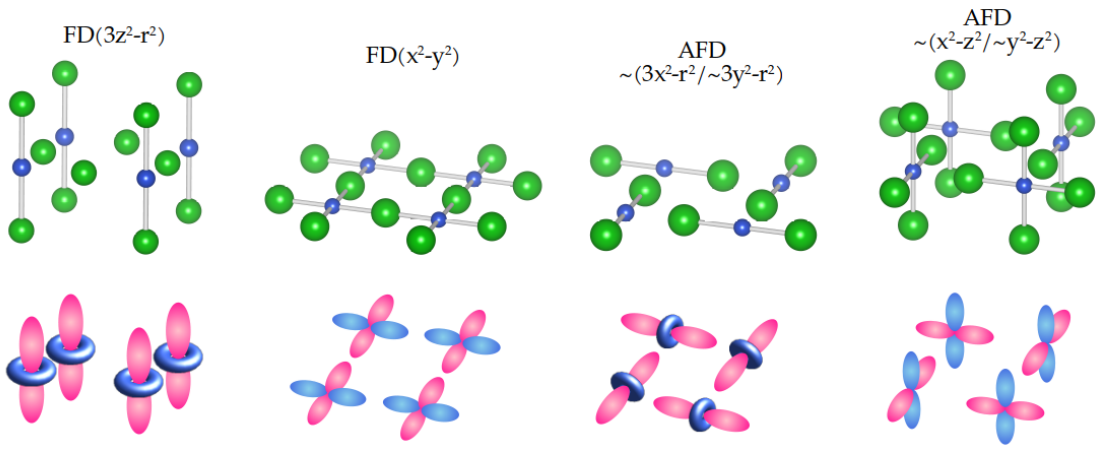

Figure 1.4: Four types of orbital orderings in CuF_2 and CuO_2 planes. In the case of AFD orderings the symbol $\sim$ means that these orbitals do not have a pure character since the wave functions are modified by the orthorhombic distortion.

The FD($3z^2 - r^2$) phase in K_2CuF_4 is unstable due to PJT effect, where the instability is driven by changes in the electron density, and thus, in bond covalence. This effect leads to orthorhombic distortions of the complexes and the consequent change in the orbital ordering from FD to AFD($\sim 3x^2 - z^2/\sim 3y^2 - z^2$) [19]. The symmetry of the system is reduced from tetragonal I4/mmm to orthorhombic Cmca, which is followed by a change in the magnetic order of this system, from AFM in the parent phase to FM in the orthorhombic experimental phase. The situation is analogue in Cs_2AgF_4. By contrast, in La_2CuO_4, the orbital ordering remains FD($x^2 - y^2$) after the distortion to Cmca phase (tilting of CuO_6^{8-} complexes) as well as the AFM order.

As shown by García-Fernández et al. in [19], in noncubic insulating crystals containing d^9 transition-metal ions without orbital degeneration, understanding orbital ordering and distortions requieres to go beyond the concept of superexchange and KK model. For both K_2CuF_4 and La_2CuO_4, it was found that the orbital ordering is determinated by the electrostatic potential created by the rest of lattice ions over the MX_6 complexes. Taking these facts into account, one of our objectives is to extend these results by including the magnetic order in both parent and experimental phases.

In order to analyse these facts we perform first- and second-principles simulations in both FM and AFM states of high- and low-symmetry phases. The procedure is as follows: (1) Examination of structure and magnetism of both parent and experimental phases (Section 5.1). (2) Calculation of the distortion from parent to experimental phase (Section 5.2). (3) Analysis of the band structure from first- and second-principles (Section 5.3). (4) To study the emergence of ferroelasticity under distortion-induced strain (Section 5.4)

2. First- and second-principles calculations

One of the main problems in condensed matter physics is understanding and predicting the properties of materials. The fundamental basis of a wide range of phenomena in materials can be understood by their electronic structure [23]. Over the last decades, computational simulations have proven to be succesful in determining the electronic structure of a large amount of materials and, therefore, in predicting the behaviour of these systems.

In this work we have employed first-principles simulations to analyse crystalline and magnetic structures of different solids, with the main purpose of uncovering the underlying mechanism that leads to experimental observations. It is worth noting the importance of first-principles simulations in order to obtain the parent phase of systems affected by vibronic coupling (Section 3), although this phase is not stable and cannot be observed experimentally.

This section gives a general overview of first-principles calculations, as well as the fundamentals of density functional theory (DFT), one of the most widely used theoretical framework in solids simulations today (Section 2.2). The description of the software used and details of the calculations performed are included in Section 2.3. In first-principles simulations the stationary Schrödinger equation is solved for fixed nuclei, which enables predicting materials properties using just fundamental constants. These calculations provide accurate energies and equilibrium geometries but are limited to hundreds of atoms due to the computational scaling. Furthermore, first-principles are constrained to T = 0 K, so cannot provide insight into the effects of temperature. In order to solve these issues, a first-principles-based (second-principles) scheme can be used, which allows simulating large-scale materials. Second-principles methods draw from the fact that material response to perturbations usually involves a set of electrons and holes. These active electrons or holes are separated from the others and treated as the basic object of the calculations, by contrast to first-principles, where the basic units are all individual atoms. In Section 2.4, a brief description of second-principles methods is included. In this work, a model of second principles, which provides similar results to those obtained from first-principles calculations, have been employed in order to interpret the band structure of layered perovskites.

Regarding notation, nuclei position vectors are written with upper case letters $\{\vec{R}\}$ while electrons position vectors with lower case $\{\vec{r}\}$, where the braces indicate a multielectronic system. All equations are expressed in atomic units, i.e., $e = \hbar = m = 1$.

2.1. First principles methods

In non-relativistic regime, which can be assumed for most material properties [24], the wave function associated with the electron distribution of the system is governed by the time-independent Schrödinger equation.

$$H\psi(\{\vec{R}\},\{\vec{r}\}) = E\psi(\{\vec{R}\},\{\vec{r}\}) \tag{2.1}$$

Equation 2.1 is an eigenvalue problem and should be solved to determine the eigenfunction ψ, from which the properties of the system could be obtained. The wave function ψ depends of both nuclei $\{\vec{R}\} = \{\vec{R}_1, \vec{R}_2, ...\}$ and electrons $\{\vec{r}\} = \{\vec{r}_1, \vec{r}_2, ...\}$ position vectors, E is the total energy of the stationary state ψ and H is the Hamiltonian operator, which can be written as the sum of potential and kinetic energies of electrons and nuclei.

$$H = -\frac{1}{2}\sum_i \vec{\nabla}^2_{\vec{r}_i} - \sum_I \frac{1}{2M_I}\vec{\nabla}^2_{\vec{R}_I} + \frac{1}{2}\sum_{i,j}\frac{1}{\vec{r}_i - \vec{r}_j} + \frac{1}{2}\sum_{I,J}\frac{Z_I Z_J}{\vec{R}_I - \vec{R}_J} - \frac{1}{2}\sum_{i,I}\frac{Z_I}{\vec{R}_I - \vec{r}_i} \quad (2.2)$$

where electrons and nuclei are indicated by lower case and upper case subscripts respectively. The presence of many body terms in Equation 2.2 prevents the analytical resolution of Equation 2.1. Furthermore, even in small molecules, numerical resolution is extremely costly and, therefore, further approximations are required.

The first step to solve numerically Equation 2.1 is through the Born-Oppenheimer adiabatic approximation, which decouples the motion of electrons and nuclei, taking into account that the mass of the latter is much higher than that of the former. Therefore, electrons and nuclei are considered as independent so the wave function can be written as the product of electronic and nuclear contributions, $\psi(\{\vec{R}\},\{\vec{r}\}) = \psi_i(\{\vec{r}\})\psi_n(\{\vec{R}\})$. Then, the Hamiltonian can be redefined as the sum of kinetic energy of nuclei and the electronic Hamiltonian H_e.

$$H = -\sum_I \frac{1}{2M_I}\vec{\nabla}^2_{\vec{R}_I} + H_e \quad (2.3)$$

where the electronic Hamiltonian can be written as follows

$$H_e = -\frac{1}{2}\sum_i \vec{\nabla}^2_{\vec{r}_i} + \frac{1}{2}\sum_{i,j}\frac{1}{\vec{r}_i - \vec{r}_j} + \frac{1}{2}\sum_{I,J}\frac{Z_I Z_J}{\vec{R}_I - \vec{R}_J} - \frac{1}{2}\sum_{i,I}\frac{Z_I}{\vec{R}_I - \vec{r}_i} \quad (2.4)$$

In these conditions, we can determined electronic and nuclear wave functions in two steps:

1. Electronic dynamics with fixed nuclei: the electronic equation that describe the movement of electrons when nuclei are frozen is solved

$$H_e\psi_i(\{\vec{r}\}) = E_i(\{\vec{R}\})\psi_i(\{\vec{r}\}) \quad (2.5)$$

   Equation 2.5 is a differential equation where the eigenvalue E_i depends parametrically of nuclear coordinates [24]. This equation is solved for different fixed nuclear coordinates obtaining the corresponding energies, which define the adiabatic potential energy surface (APES).

   All systems have infinite electronic states and, in general, electronic equation contains terms that couple them. These terms are important for systems with electronic surfaces that are close in energy. In the framework of adiabatic approximation these coupling terms are neglected, so the total wave function is restricted to one electronic surface [24].

2. Nuclear dynamics under electronic potential: once the electronic wave function has been determined, nuclear dynamics under electronic potential are calculated. The wave function of nuclei is obtained by solving the nuclear equation

$$\left[-\sum_i \frac{1}{2M_I}\vec{\nabla}^2_{\vec{R}_I} + E_i(\{\vec{R}\})\right]\psi_n(\{\vec{R}\}) = E(\{\vec{R}\})\psi_n(\{\vec{R}\}) \quad (2.6)$$

Within the adiabatic approximation, nuclear wave function is obtained solving Equation 2.6 under the potential of a single APES, $E_i(\{\vec{R}\})$. This implies the approximation of independent APES and therefore, adiabatic approximation is not valid for systems whose APES have similar energies.

The total energy $E(\{\vec{R}\})$ of the state is then the sum of the energy of the vibrational state $E_\nu(\{\vec{R}\})$ and the energy of the electronic state $E_i(\{\vec{R}\})$.

Nevertheless, the resolution of Equation 2.5 implies the determination of the many-electron wave function $\psi_i(\{\vec{r}\})$, that can be obtained analytically just for one electron systems due to the cross terms of the electronic Hamiltonian and, additionally, numerical calculation is extraordinarily costly. In order to fix this issue, another approach is introduced. We will assume that electrons are independent particles except for the fact that they fulfilled Pauli exclusion principle. The Hartree-Fock method, which is the basis of all electronic structure techniques, provides the ground state energy for a single configuration, through the variational principle. The procedure consists of varying a set of trial electronic wave functions ψ_t until the minimum energy is reached.

In HF method the total wave function is the antisymmetrized product of single-electron wave functions, which are usually the atomic orbitals $\phi_i(\vec{r_j})$, so electron correlation is neglected. The total wave function can be written in terms of a Slater determinant

$$\psi_i(\{\vec{r}\}) = \begin{vmatrix} \phi_1(\vec{r}_1) & \phi_2(\vec{r}_1) & ... & \phi_n(\vec{r}_1) \\ \phi_1(\vec{r}_2) & \phi_2(\vec{r}_2) & ... & \phi_n(\vec{r}_2) \\ \vdots & \vdots & \ddots & \vdots \\ \phi_1(\vec{r}_n) & \phi_2(\vec{r}_n) & ... & \phi_n(\vec{r}_n) \end{vmatrix} \tag{2.7}$$

In general, current non-interacting electron approximations incorporate an effective potential to the non-interacting Hamiltonian that includes somehow the effect of electron correlation. This can be done following two different paths: perturbation theory or variational methods. In perturbation theory based methods, the correlation associated to electron-electron interaction is included as a perturbation of electronic wave function. Among variational models there are two main techniques: coupled-cluster, in which the many-electron wave function is built with the exponential cluster operator and configuration interaction, where a linear combination of Slater determinants introduce the excited states of the system.

Indeed, electron correlation constitutes one of the greatest challenges in material simulations. One of its main consequences is the well-known exchange interaction, which is the underlying cause of magnetism. Metal-insulator transitions, high-temperature superconductivity and other relevant effects also emerge from correlations. The major problem comes from systems in which the strong electron correlation requires accurate descriptions that must go beyond the effective non-interacting electrons scheme. This sort of materials are often in the boundary between localized and delocalized, involving 3d and 4d transition metals as well as 4f and 5f rare earths [23]. Despite this fact, independent-electron approaches are usually accurate enough to describe correlation effects. Unfortunately, post-HF methods, as the described in the previous paragraph, are extremely computationally expensive. In this cases, density functional theory plays a key role in simulating materials where the correlation is weak or relatively moderate. In Section 2.2 the fundamental basis and theorems of DFT are explained.

2.2. Density functional theory

Currently, DFT is the most used technique in first-principles calculations of molecules and especially in solids due to the limitations of post-HF methods. Post-HF methods are based on the many-electron wave function $\psi(\{\vec{r}\})$ which is a complex object, it is not a physical observable and it depends on the vector position of each electron ($3N$ dimensional, where N is the number of electrons). By contrast, the main idea of DFT is considering the electron density $n(\vec{r})$ instead of the wave function [25].

$$n(\vec{r}) = \int d^3\vec{r}_2 ... \int d^3\vec{r}_N |\psi(\{\vec{r}_1, \vec{r}_2, ...\vec{r}_N\})|^2 \tag{2.8}$$

The electron density is a positive function, an observable and involves just the position vector of the point considered $\vec{r} = (x, y, z)$. Furthermore, it contains all the information of the state of the system, such as the wave function.

Density functional theory is based in two theorems for systems with non-degenerate ground states proven by Hohenberg and Kohn and generalised by Levy and Lieb [23], [25]. These theorems can be applied to any system of interacting particles in an external potential $V_{ext}(\vec{r})$, for which the Hamiltonian can be written as follows

$$H = -\frac{1}{2}\sum_i \vec{\nabla}^2_{\vec{r}_i} + \frac{1}{2}\sum_{i,j}\frac{1}{|\vec{r}_i - \vec{r}_j|} + \sum_i V_{ext}(\vec{r}_i) \tag{2.9}$$

Theorem I. For any system of interacting electrons in an external potential $V_{ext}(\vec{r})$, the external potential is uniquely determined by the ground state density, except for an additive constant.

Corollary I. All properties of the system are determined given the ground state density $n_0(\vec{r})$, since the Hamiltonian and the many-electron wave function for all states are fully determined.

Theorem II. A universal functional for the energy in terms of the electron density $E[n]$ can be defined and it is valid for any external potential. For any particular $V_{ext}(\vec{r})$ the exact energy of the ground state is the global minimum of this functional and the density that minimizes the energy functional is the ground state density $n_0(\vec{r})$.

Corollary II. The functional $E[n]$ is enough to determine the exact ground state density and energy.

As mentioned above, Hohenberg and Kohn theorems were originally applied to non-degenerate ground states. Currently, it has been proved that DFT is also valid for degenerate states and for the lowest energy excited states.

2.2.1. Kohn-Sham approach

Hohenberg and Kohn theorems make important statements about electron density and its functional, but they are not helpful in finding it. Regarding the resolution of practical problems, Kohn and Sham proposed a model to obtain the energy of the ground state within the one-electron approach, as well as to estimate the electron correlation in order to minimize errors [24].

Kohn-Sham (KS) model considers a fictitious system S of non-interacting electrons which feel the external potential $v_{ext}(\vec{r})$. This system has the same density as the real system.

Therefore, the total energy of the real system can be written as follows

$$E[n] = T_S[n] + J_S[n] + E_{XC}[n] + \int n(\vec{r_i}) v_{ext}(\vec{r}) d^3\vec{r} \tag{2.10}$$

where $T_S[n]$ is the kinetic energy of non-interacting electrons, $J_S[n]$ is the Coulomb energy term of system S and $E_{XC}[n]$ is the exchange-correlation energy, which represents the difference between the independent-electron system S and the real system. It is given by

$$E_{XC}[n] = T[n] - T_S[n] + E_{ee}[n] - J_S[n] \tag{2.11}$$

where $T[n] - T_S[n]$ is the correlation due to kinetic energy and $E_{ee}[n] - J_S[n]$ represents the exchange, electron-electron correlation and autointeraction correction.

If $E_{XC}[n]$ of Equation 2.11 was known the exact ground state density and energy of the many-electron system could be found by solving the system of KS equations [23].

$$\left[-\frac{1}{2}\nabla^2 + V_{KS}(\vec{r})\right] \phi_i(\vec{r}) = \varepsilon_i \phi_i(\vec{r}) \tag{2.12}$$

where the eigenvalues ε_i and eigenvectors ϕ_i are the one-electron energies and wave functions respectively. The effective potential $V_{KS}(\vec{r}) = V_{ext}(\vec{r}) + \int \frac{n(\vec{r_i})'}{|\vec{r}-\vec{r}'|} d\vec{r}' + V_{XC}(\vec{r})$ involves the electron-nucleus interaction, electron-electron repulsion and the exchange-correlation term. This term is given by the derivative of $E_{XC}[n]$ (Equation 2.11) with the density $n(\vec{r})$.

In Equation 2.12, the only approximation is the exchange-correlation potential, which is, in general, a small correction to the functional, since most of kinetic energy is included in $T_S[n]$ and most of electronic repulsions are accounted by $J_S[n]$ (Equation 2.11). In practical problems the exchange-correlation functional is approximated in such a way that calculations are relatively fast but keeping the suitable accuracy so that effects where energy differences are around 10-100 meV (for example magnetism) can be reproduced.

2.2.2. Spin-unrestricted KS DFT

Since we are dealing with open shell ions, DFT should be extended in order to reproduce the magnetic order of the systems studied. Then, the KS wave functions are replaced by the two component Pauli wave functions ψ_i^σ [25] so the electron density is redefined as follows

$$n(\vec{r}) = \sum_\sigma n(\vec{r}, \sigma) = \sum_\sigma \sum_i^{N^\sigma} |\psi_i^\sigma(\{\vec{r}\})|^2 \tag{2.13}$$

For a system of $N = N^\uparrow + N^\downarrow$ independent electrons. This could be extended to non-collinear magnetic structures considering the density matrix instead of electron density [25], which is beyond the scope of this work.

2.2.3. Exchange-correlation functionals

In KS method we can differentiate the independent electron kinetic energy and the long-range Coulomb terms. Therefore, the remaining exchange-correlation functional can be estimated as a local or nearly local functional of electron density [23].

The first approximation of exchange-correlation functional was proposed by Kohn and Sham. They considered a homogeneous electron gas with the same electron density as the solid, so the exchange-correlation energy is given by the following integral

$$E_{XC}[n^{\uparrow}, n^{\downarrow}] = \int n(\vec{r})\varepsilon_{XC}[n^{\uparrow}(\vec{r}), n^{\downarrow}(\vec{r})]\mathrm{d}\vec{r} \tag{2.14}$$

where the exchange-correlation energy ε_{XC} at each point is the same as in the homogeneous electron gas. This is the well-known local spin density approximation (LSDA), wherein the other approaches are based on.

Local density approximation can be extended by including the gradient of the electron density, that incorporates the inhomogeneities. This is precisely the generalized gradient approximation (GGA).

There are further approximations such as LSDA+U, where U is a parameter that accounts the electronic repulsion, meta- and hiper-GGA or hybrid functionals which include some exact exchange that comes from HF theory and have been widely used in this work.

2.3. Molecular and solid simulations

The development of approximate practical methods which apply quantum theory to complex systems as molecules and solids has provided insight into important properties of these systems, as well as enables the prediction of new features and phenomena. Despite the succes of computational simulations, there are remaining limitations in terms of the balance between fulfilled the goals of accuracy and computational feasibility.

Currently, we can outline two schemes in computational simulation of materials. First, the study of materials can be done via cluster methods with appropiate embbeding. In this case, high-quality post-HF methods (coupled-cluster, configurations interaction and so on) are applied to a cluster of atoms involving the electrons that are relevant in the phenomenom studied. This cluster is embedded in a potential that accounts the crystal environment, which can be simulated by classical or quantum approaches. These methods are typically used to study reactions in surfaces, absoption/emission spectroscopy, chemical processes in solution and proteins.

On the other hand, to simulate bulk crystals, periodic calculations are the most widely used scheme. In this case, the real system is treated as infinite since the majority of bulk properties are not affected by border effects. A simulation cell is repeted in the space using Born-von Karman boundary conditions. One of the main problems of these simulations arises when larger size cells are required. For example, in DFT codes, the computational cost scales with N^3 and thus, doubling the size of the simulation cell will make the calculation 8 times slower.

2.3.1. Software

Crystal code

Periodic simulations on AgF_2 and layered systems K_2CuF_4, Cs_2AgF_4 and La_2CuO_4 were carried out using Crystal17 package which performs ab initio calculations where HF and KS Hamiltonians can be employed. The fundamental approximation of this code is the expansion of single-electron wave function as linear combination of Bloch functions described in terms of local functions. These local functions are, in turn, linear combinations

of Gaussian type functions (GTF), whose shape is defined in the basis set section of the input. The program enables the use of sp shells which might improve the speed of the calculations [26].

Crystal17 is able to handle the symmetry of the space group of the materials in all steps of the calculations, which implies an advantage over other codes in saving CPU time, especially for high-symmetry solids. Furthermore, the full use of symmetry allow us to fix the space group and, consequently, we can determine the parent phase of a distorted structure. On the other hand, the high efficiency in the implementation of hybrid functionals contributes to speed up calculations.

All ions have been described using high quality triple-ζ polarized basis sets taken directly from Crystal website [27] together with the hybrid exchange-correlation functional PW1PW, a mixing of a GGA functional involving with 20% of HF exchange. This combination has been widely shown to provide accurate results in predicting crystal structures and properties for a broad range of materials.

Since we are dealing with open shell Ag^{2+} and Cu^{2+} ions all calculations have been performed under the framework of spin unrestricted Kohn-Sham DFT. Tight convergence criteria for energy changes (10^{-8}-10^{-9} a.u.) and RMS for both gradient and atomic displacements (0.0001-0.0002 a.u.) have been imposed in geometry optimizations. Furthermore, both FM and AFM states were studied within a model of collinear spins.

The first step in the simulation of all systems was the geometry optimization of the experimental structures, i.e., orthorhombic Pbca in the case of AgF_2 and Cmca in layered perovskites. The calculated values agree with the experimental ones within 2% of error in all cases. The magnetic order of the lowest energy state on each system coincides with the experimental one.

The next step was the optimization of the parent phases. In AgF_2 the reference phase was obtained by replacing all open shell ions Ag^{2+} by closed shell Cd^{2+} ions. Then, the system undergoes a transition to the cubic $Pa\bar{3}$ phase, where AgF_6^{4-} complexes exhibit trigonal symmetry. In order to study the distortion from this parent phase, we introduce a single impurity of Ag^{2+} occupying a Cd^{2+} lattice site and optimize the atomic positions keeping the cell parameter of cubic phase fixed, obtaining an AgF_6^{4-} distorted complex. Calculations on primitive (12 ions) and 2x2x2 conventional supercell (96 ions) have been performed, obtaining similar metal-ligand distances.

Regarding the layered systems K_2CuF_4, Cs_2AgF_4 and La_2CuO_4 we have optimized both the low-symmetry (experimental) Cmca phase and the high-symmetry I4/mmm phase for both FM and AFM orders. Energy calculations starting from tetragonal I4/mmm phase and distorting by an orthorhombic deformation has been carried out for FM and AFM states. The calculation on I4/mmm space group were carried out using the conventional cell expanded to $\sqrt{2} \times \sqrt{2} \times 1$ supercell in order to set FM and AFM states. In addition, we have calculated the band structure and projected density of states (PDOS) in the high-symmetry phase in order to analysed in-plane and out-of-plane dispersion as well as the ground state of the system.

Amsterdam density functional code

Appart from periodic simulations, cluster calculations on AgF_2 have been carried out in order to analysed the ground state of AgF_6^{4-} units in the parent high-symmetry phase of

this system. For this goal, Amsterdan density functional (ADF) code has been employed. It is a computational chemistry program particularly used to predict strutures, reactivity and spectra of molecules and complexes, that works exclusively with DFT methods [28]. Among the advantages of ADF, the high-quality basis, the accurate numerical integration and the full use of the symmetry of the point groups of the molecules or complexes can be highlighted. The main problem of cluster calculations is the embedding, which can hinder the convergence.

The calculations over AgF_6^{4-} transition-metal complex have been performed both in vacuo (isolated complex) and considering the electrostatic potential of the rest of the lattice. The electrostatic potential has been obtained using Ewald program, which calculates the interaction energy between one electron located at thousands of points in the complex and the rest of lattice ions, which are represented as point charges. The calculation follows a self-consistent Ewald-Evjen summation, where the interaction is divided in short range and long range contributions. Then, the calculated interaction energy is fitted to a set of about 200-300 point charges around AgF_6^{4-} units.

In these calculations triple-ζ polarized basis set combined with the widely used B3LYP hybrid functional have been employed. B3LYP is a three parameters hybrid functional, which combine LDA and GGA approximations to include the electron correlation and also these two with HF to account the exchange.

2.4. Second-principles DFT

In order to perform large-scale simulations on materials considering both atomic and electronic degrees of freedom, the second-principles methodology developed by García-Fernández and coworkers [29] has been employed. This technique relies on quantum-mechanical theory (DFT) and can be systematically improved with moderate computational effort. There are other efficient schemes to simulate large-scale systems, such as quantum-mechanics molecular-mechanics (QM/MM), semiempirical methods as tight-binding DFT (DFTB) or effective Hamiltonians, based on coarse-grained treatment of the material. These methods are powerful tools for dealing with large systems. However, they are not enough accurate when the energy differences involved in the interactions are small ($\sim$ meV) or for systems that require a full atomistic description.

In such cases, a method based on first-principles can be used, enabling arbitrarily high accuracy calculations at modest computational cost. It is based on the combination of an accurate model potential which describes the dynamics of the lattice and the representation of involved electronic degrees of freedom within a tight-binding-like approach. The problems of bond breaking and formation are not well described within this approach since it assumes a fixed topology, which improves computational performance [29].

In this approach, the total electron density is divided into two contributions [29]

$$n(\vec{r}) = n_0(\vec{r}) + \delta n(\vec{r}) \tag{2.15}$$

where $n_0(\vec{r})$ is the reference density, which corresponds to the ground state density in non-magnetic systems, and $\delta n(\vec{r})$ is the deformation density, considered as a small perturbation to $n_0(\vec{r})$. In order to clarify the concepts of reference and deformation densities, the example of a electron-doped semiconductor taken from [29] is represented in Figure 2.1. The undoped phase (Figure 2.1 (e)), which corresponds to the reference atomic geometry

(RAG) and the reference electron density $n_0(\vec{r})$, is characterized by an electronic configuration in which the valence band is fully occupied and the conduction band is empty. If this system is doped, the electron cloud will tend to compensate the extra charge. The doping electron will be excited to the conduction band, as indicated in Figure 2.1 (f). The variations in the charge distribution associated with the changes in the electronic configuration are represented through deformation density $\delta n(\vec{r})$ (Figure 2.1 (c)).

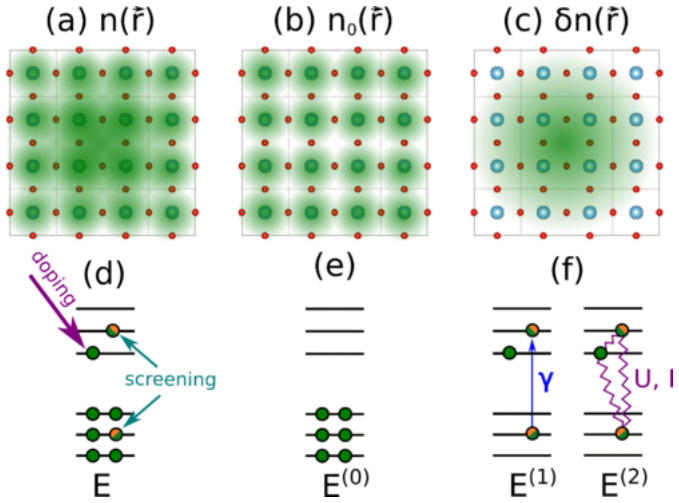

Figure 2.1: Sketch that represents the division of electron density used in second-principles simulations for an electron-doped semiconductor. Top panels (a)-(c) represents the atomic geometry (blue and red balls) and electron density (green clouds) for (a) total electron density $n(\vec{r})$, (b) reference density $n_0(\vec{r})$ and (c) deformation density $\delta n(\vec{r})$. Bottom panels (d)-(f) illustrate the one-electron levels for each atomic geometry and electron density. Reprinted from [29].

The division of electron density is used to expand the full DFT energy up to second order

$$E_{\mathrm{DFT}} \approx E^{(0)} + E^{(1)} + E^{(2)} \tag{2.16}$$

where $E^{(0)}$ is the full DFT energy for the reference density, which is the dominant contribution and is valid for any geometry of the lattice [29]. The first order term $E^{(1)}$ involves the electron-lattice term (including JT) and the second order term $E^{(2)}$ accounts the electron-electron interactions. Both terms are related with the deformation density $\delta n(\vec{r})$.

The electron density can be written in terms of Wannier functions $\chi_a(\vec{r})$ and $\chi_b(\vec{r})$ [29]

$$n(\vec{r}) = \sum_{ab} d_{ab}\chi_a(\vec{r})\chi_b(\vec{r}) \tag{2.17}$$

where d_{ab} is the reduced density matrix, henceforth the occupation matrix. The reference density $n_0(\vec{r})$ and the deformation density $\delta n(\vec{r})$ can be also expressed in the basis of Wannier functions

$$n_0(\vec{r}) = \sum_{ab} d^{(0)}_{ab}\chi_a(\vec{r})\chi_b(\vec{r}) \tag{2.18}$$

$$\delta n(\vec{r}) = \sum_{ab} D_{ab}\chi_a(\vec{r})\chi_b(\vec{r}) \tag{2.19}$$

where the deformation occupation matrix is $D_{ab} = d_{ab} - d_{ab}^{(0)}$. Using these definitions, the total energy for magnetic systems can be expressed as follows

$$E \approx E^{(0)} + \sum_{ab}(D_{ab}^{\uparrow} + D_{ab}^{\downarrow})\gamma_{ab} + \frac{1}{2}\sum_{ab}\sum_{a'b'}[(D_{ab}^{\uparrow} + D_{ab}^{\downarrow})(D_{a'b'}^{\uparrow} + D_{a'b'}^{\downarrow})U_{aba'b'} - (D_{ab}^{\uparrow} - D_{ab}^{\downarrow})(D_{a'b'}^{\uparrow} - D_{a'b'}^{\downarrow})I_{aba'b'}] \tag{2.20}$$

It should be highlighted that Equation 2.20 is formally equivalent to the HF expression of the energy [24] written in terms of density matrices. The second term of this equation is the electron-lattice contribution $E^{(1)}$ and the double summation is the electron-electron contribution $E^{(2)}$. The parameter γ_{ab} can be obtained from the one-electron operator

$$\gamma_{ab} = \langle \chi_a | \hat{h}_0 | \chi_b \rangle \tag{2.21}$$

while Hubbard-like $U_{aba'b'}$ and Stoner-like $I_{aba'b'}$ parameter comes from the two-electron integrals of Equations 2.22 and 2.23 [29]

$$U_{aba'b'} = \langle \chi_a \chi_{a'} | \hat{g}_U | \chi_b \chi_{b'} \rangle \tag{2.22}$$

$$I_{aba'b'} = \langle \chi_a \chi_{a'} | \hat{g}_I | \chi_b \chi_{b'} \rangle \tag{2.23}$$

$$g_U(\vec{r}, \vec{r'}) = \frac{1}{|\vec{r} - \vec{r'}|} + \frac{1}{2}\left[\left.\frac{\delta^2 E_{xc}}{\delta n(\vec{r},\uparrow)\delta n(\vec{r'},\downarrow)}\right|_{n_0} + \left.\frac{\delta^2 E_{xc}}{\delta n(\vec{r},\uparrow)\delta n(\vec{r'},\uparrow)}\right|_{n_0}\right] \tag{2.24}$$

$$g_I(\vec{r}, \vec{r'}) = \frac{1}{2}\left[\left.\frac{\delta^2 E_{xc}}{\delta n(\vec{r},\uparrow)\delta n(\vec{r'},\downarrow)}\right|_{n_0} - \left.\frac{\delta^2 E_{xc}}{\delta n(\vec{r},\uparrow)\delta n(\vec{r'},\uparrow)}\right|_{n_0}\right] \tag{2.25}$$

The one-particle Hamiltonian associated with spin channel σ, separating γ_{ab} and $U_{aba'b'}$ in short (sr) and long (lr) range terms is given by

$$h_{ab}^{\sigma} = h_{ab}^{lr} + \gamma_{ab}^{sr}\sum_{a'b'}[(D_{a'b'}^{\sigma} + D_{a'b'}^{-\sigma})U_{aba'b'}^{sr} - (D_{a'b'}^{\sigma} - D_{a'b'}^{-\sigma})I_{aba'b'}] \tag{2.26}$$

where the long range terms have been included in a term that comes from the expansion of a far-field electrostatic interaction [29]. Therefore, given a model for the material, its state is defined by the density matrix.

In this scheme, the dependence of the model parameters on the atomic configuration is captured by the electron-lattice coupling terms. The relation between the short range self-term γ_{ab}^{sr} and the atomic configuration is as follows

$$\gamma_{ab}^{sr} = \gamma_{ab}^{\mathrm{RAG},sr} + \sum_{\lambda\upsilon}\left[-\vec{f}_{ab,\lambda\upsilon}^{T}\delta\vec{r}_{\lambda\upsilon} + \sum_{\lambda'\upsilon'}\delta\vec{r}_{\lambda\upsilon}^{T}\overleftrightarrow{g}_{ab,\lambda\upsilon\lambda'\upsilon'}\delta\vec{r}_{\lambda'\upsilon'} + ...\right] \tag{2.27}$$

where $\vec{f}$ and $\overleftrightarrow{g}$ are the first and second-rank tensors that characterize the electron-lattice coupling, closely related to vibronic constants F_I and F_{IJ} (Section 3.1). In addition, $\gamma_{ab}^{\mathrm{RAG},sr}$ is the self term in the reference atomic geometry (RAG) and $\delta\vec{r}_{\lambda\upsilon}$ quantifies the atomic displacement of atoms λ and υ

$$\delta\vec{r}_{\lambda\upsilon} = \overleftrightarrow{\eta}(\vec{R}_{\Upsilon} - \vec{R}_{\Lambda} + \vec{\tau}_{\upsilon} - \vec{\tau}_{\lambda}) + \vec{u}_{\upsilon} - \vec{u}_{\lambda} \tag{2.28}$$

where $\overleftrightarrow{n}$ is the homogeneous strain tensor, $\vec{R}_\Upsilon$ and $\vec{R}_\Lambda$ the lattice vector of cells Υ and Λ, $\vec{\tau}_\upsilon$ and $\vec{\tau}_\lambda$ the position of atoms υ and λ in the reference geometry and $\vec{u}_\upsilon$ and $\vec{u}_\lambda$ the absolute displacements of atoms υ and λ in their cells with respect to the strained reference structure [29].

The last step in this section is to establish a link between the parameters of Equation 2.26 and the parameters implemented in our model. This model has been built considering the minimum number of parameters which will be determined by means of symmetry considerations. These parameters can be grouped in three sets: (1) self-terms γ_{ab}, (2) electron-lattice terms and (3) electron-electron terms.

Regarding (1) self-terms, it is important to note that in this simple model only $3z^2-r^2$, x^2-y^2 metal orbitals as well as p orbitals of equatorial ligands are included. Therefore, the one-electron terms γ_{ab} in the Slater-Koster tight-binding scheme, which assumes atomic-like orbitals (χ_α, χ_β) are $\gamma_{ab} = \langle\phi_a|\hat{h}|\phi_b\rangle \approx \langle\chi_\alpha(\vec{r})Y_{m,l}|\hat{h}|\chi_\beta(\vec{r})Y_{m',l'}\rangle$. This approach considers fixed interatomic distance $\vec{r}_{a,b}$, which in our model is the metal-ligand distance in the parent phase (RAG). It can be expressed in terms of direction cosines to the neighboring atom

$$\vec{r}_{a,b} = (r_x, r_y, r_z) = d(l, m, n) \tag{2.29}$$

Taking these considerations into account, the interatomic matrix elements involved in our model are the self terms $\gamma_{3z^2-r^2}$, $\gamma_{x^2-y^2}$, γ_p, since γ_{ab} are expanded on atomic positions, and the terms which describe the interaction between metal and ligand orbitals [30]

$$\begin{aligned}
\gamma_{3z^2-r^2,p_x} &= l\left(n^2 - \frac{l^2+m^2}{2}\right)V_{pd\sigma}^{\mathrm{RAG}} - \sqrt{3}ln^2V_{pd\pi}^{\mathrm{RAG}} \\
\gamma_{3z^2-r^2,p_y} &= m\left(n^2 - \frac{l^2+m^2}{2}\right)V_{pd\sigma}^{\mathrm{RAG}} - \sqrt{3}mn^2V_{pd\pi}^{\mathrm{RAG}} \\
\gamma_{3z^2-r^2,p_z} &= n\left(n^2 - \frac{l^2+m^2}{2}\right)V_{pd\sigma}^{\mathrm{RAG}} + \sqrt{3}n(l^2+m^2)V_{pd\pi}^{\mathrm{RAG}} \\
\gamma_{x^2-y^2,p_x} &= \frac{\sqrt{3}}{2}l(l^2-m^2)V_{pd\sigma}^{\mathrm{RAG}} + l(1-l^2+m^2)V_{pd\pi}^{\mathrm{RAG}} \\
\gamma_{x^2-y^2,p_y} &= \frac{\sqrt{3}}{2}m(l^2-m^2)V_{pd\sigma}^{\mathrm{RAG}} - m(1+l^2-m^2)V_{pd\pi}^{\mathrm{RAG}} \\
\gamma_{x^2-y^2,p_z} &= \frac{\sqrt{3}}{2}n(l^2-m^2)V_{pd\sigma}^{\mathrm{RAG}} - n(l^2-m^2)V_{pd\pi}^{\mathrm{RAG}}
\end{aligned} \tag{2.30}$$

Taking into account the symmetry, the expressions in Equation 2.30 are reduced to

$$\begin{aligned}
\gamma_{3z^2-r^2,p_x} &= -\frac{V_{pd\sigma}^{\mathrm{RAG}}}{2} \\
\gamma_{3z^2-r^2,p_y} &= -\frac{V_{pd\sigma}^{\mathrm{RAG}}}{2} \\
\gamma_{3z^2-r^2,p_z} &= V_{pd\sigma}^{\mathrm{RAG}} \\
\gamma_{x^2-y^2,p_x} &= \frac{\sqrt{3}}{2}V_{pd\sigma}^{\mathrm{RAG}} \\
\gamma_{x^2-y^2,p_y} &= -\frac{\sqrt{3}}{2}V_{pd\sigma}^{\mathrm{RAG}} \\
\gamma_{x^2-y^2,p_z} &= 0
\end{aligned} \tag{2.31}$$

Therefore, the one-electron terms of our model are $\gamma_{3z^2-r^2}$, $\gamma_{x^2-y^2}$, γ_p and $V_{pd\sigma}^{\mathrm{RAG}}$, where the last one corresponds to the reference geometry, i.e., the parent phase. However, metal-ligand interaction changes with the interatomic distance, and its dependence is accounted by (2) electron-lattice coupling term (Equation 2.27), included in the model as a fifth parameter

$$V_{pd\sigma} = V_{pd\sigma}^{\mathrm{RAG}} - \vec{f}\delta\vec{r}_{a,b} \tag{2.32}$$

where we have assumed that the quadratic contribution is zero.

Finally, the next step is parametrizing the four-index integrals that accounts (3) electron-electron interactions. This parametrization has been implemented following ligand-field theory, which assumes spherical symmetry to calculate electron-electron interactions within the d-shell, since in transition-metal complexes these orbitals are compact [30]. The matrix elements within this assumption when d-orbitals are expressed in spherical harmonics are as follows

$$\langle \chi_\alpha \chi_{\alpha'} | \hat{g} | \chi_\beta \chi_{\beta'} \rangle = \sum_{k=0,2,4} a_k(\alpha, \beta, \alpha', \beta') F^k \tag{2.33}$$

where $\hat{g}$ is the electron-electron interaction operator, which for magnetic systems is given by

$$\hat{g}(\vec{r}, \vec{r}', \sigma, \sigma') = \frac{1}{|\vec{r} - \vec{r}'|} + \left. \frac{\delta^2 E_{XC}}{\delta n(\vec{r}, \sigma) \delta n(\vec{r}', \sigma')} \right|_{n_0} \tag{2.34}$$

This approach reduces the number of parameters from 5^4 to 3, that are the so-called Racah parameters (A, B, C) or Slater integrals (F^0, F^2, F^4) which can be approximated by the LDA+U parameters U and J, implemented in our model

$$\begin{aligned} F^0 =& A + \frac{7}{5}C = U \\ F^2 =& 49B + 7C \approx \frac{5390}{637}J \\ F^4 =& \frac{441}{35}C \approx \frac{3528}{637}J \end{aligned} \tag{2.35}$$

In Equation 2.35, U is the screened Coulomb parameter, that accounts the interaction between the localized electrons in the system, for example the d electrons in transition-metal complexes, considering the screening from other types of electrons (p or s) and J is the screened exchange paramenter [31].

3. Vibronic coupling and magnetism

There are many phenomena and properties of molecules and solids whose study requires going beyond adiabatic approximation, considering the interaction between electrons and atomic vibrations. This interaction is known as vibronic coupling or electron-phonon coupling. The term vibronic comes from the contraction of vibrational and electronic. The quantitative evaluation of vibronic coupling problems requires the description of more than one electronic states, which implies the use of multi-reference calculation methods, which are not computationally feasible except for small molecules. In Section 3.1, vibronic coupling is simply described in the general framework of adiabatic approximation, introducing it as a perturbative correction to the adiabatic problem. Thus, this description leads to approximate solutions.

Among the variety of vibronic coupling effects in condensed matter, we are focused on the case of solids containing open shell transition-metal ions (M = Cu^{2+}, Ag^{2+}) coordinated by anions (L = F^-, O^{2-}) as first neighbours. In this configuration the valence electrons are localized (typically more than 95% of electron density) inside the complex. The common feature among these systems is the existence of a parent phase (or reference phase), whose analysis is fundamental to understand the subtleties of vibronic coupling and hence its ground state and features.

Electron-phonon coupling is a mechanism of symmetry breaking, which is one of the most active studies in physics. Under certain conditions, which will be explained below, vibronic coupling can reduce the symmetry of the parent phase. This symmetry breaking gives rise to the crystalline and magnetic structures observed in experiments and, therefore, is a key element in the analysis carried out in this work.

3.1. Fundamentals of vibronic interactions

As mentioned above, a key element in electron-phonon coupling problems is the concept of parent phase, which characterizes the state of the system before considering the vibronic coupling. In terms of electron density, in the parent phase, the asymmetric density of open shell M ions is replaced by a symmetric density of closed shell ions. In later sections we well discuss how this can be done through first-principles calculations.

At the end of this section, we will see that the structural distortions produced when vibronic coupling is considered can be divided into totally symmetric, which does not reduced the symmetry of the parent phase, and purely vibronic, that can cause a spontaneous symmetry breaking. As usually done in electron-phonon problems, where the distortions are characterized by vibrational modes, atomic positions are expressed in terms of the symmetrized coordinates Q of the normal modes, whose relation with cartesian coordinates $\vec{R}$ depends on the symmetry of the system. Therefore, the parent phase is defined by $Q = 0$.

As seen in Section 2, the state of a system is governed by the time-independent Schrödinger equation (Equation 2.1). In order to solve this eigenvalue problem, adiabatic approximation is applied. In the framework of this approach, the terms that couple different electronic states are neglected, restricting the solution to one APES. If the resolution of the problem involves more than one electronic surface this approximation cannot, in principle, be applied. In these conditions we should solve the system of coupled equations, which is extremely complex. Instead of this *diabatic* resolution, the most widely used method to deal with electron-nuclear interaction is by introducing the vibronic coupling as a perturbation

of the Hamiltonian [32]

$$H = H_r + H_Q + V(\vec{r}, Q) \tag{3.1}$$

where $\vec{r}$ in this section refers to electrons position vectors $\vec{r} = \{\vec{r}\} = \{\vec{r}_1, \vec{r}_2, ...\}$, H_r is the electronic Hamiltonian, H_Q the kinetic energy of the nuclei and $V(\vec{r}, Q)$ represents the electron-nuclear and nuclear-nuclear interactions, that can be expanded in Taylor series of small displacements of the nuclei around point $Q = 0$, which is the nuclear configuration in the high-symmetry phase

$$V(\vec{r}, Q) = V(\vec{r}, 0) + \sum_I \left(\frac{\partial V}{\partial Q_I}\right)_{Q=0} Q_I + \frac{1}{2}\sum_{I,J}\left(\frac{\partial^2 V}{\partial Q_I \partial Q_J}\right)_{Q=0} Q_I Q_J + ... \tag{3.2}$$

In a first step, we introduce the term $V(\vec{r}, 0)$, which represents the potential energy of electrons in the field of frozen nuclei [32], in the electronic equation (Equation 2.5). Thus, the energies $E_i(0)$ and eigenfunctions $\psi_i(\vec{r})$ are obtained

$$[H_r + V(\vec{r}, 0)]\psi_i(\vec{r}) = E_i(0)\psi_i(\vec{r}) \tag{3.3}$$

Equation 3.3 is equivalent to Equation 2.5 changing the nuclear coordinates from cartesian $\vec{R}$ to normal Q.

Once the electronic equation in the field of fixed nuclei is solved, we will see how these solutions change with small displacements of the nuclei. For this goal, the *vibronic coupling operator* $W(\vec{r}, Q)$ is defined [32]

$$\begin{aligned} W(\vec{r}, Q) =& V(\vec{r}, Q) - V(\vec{r}, 0) \\ =& \sum_I \left(\frac{\partial V}{\partial Q_I}\right)_{Q=0} Q_I + \frac{1}{2}\sum_{I,J}\left(\frac{\partial^2 V}{\partial Q_I \partial Q_J}\right)_{Q=0} Q_I Q_J + ... \end{aligned} \tag{3.4}$$

In order to obtain the vibronic corrections $E^\nu(Q)$ to the total energy $E_i(Q) = E_i(0) + E^\nu(Q)$ the vibronic coupling matrix should be diagonalized in the basis of electronic functions $\psi_i(\vec{r})$. It is important to noted that this resolution implies the approximation of frozen electronic wavefunctions throughout the distortion Q. The matrix elements can be expressed as follows

$$W_{ij} = \langle \psi_i(\vec{r}) | W(\vec{r}, Q) | \psi_j(\vec{r}) \rangle \tag{3.5}$$

These matrix elements are the so-called *vibronic constants* that characterized the coupling between the electronic states ψ_i and the nuclear displacements from the reference high-symmetry configuration, i.e., the effect of nuclear vibrations in the electron distribution. If we consider the first term of the vibronic coupling operator in Equation 3.4, the linear vibronic constant is given by

$$W_{ij}^{(1)} = \left\langle \psi_i^{(0)} \left| \left(\frac{\partial V}{\partial Q_I}\right) \right| \psi_j^{(0)} \right\rangle = F_I \tag{3.6}$$

The corresponding energy term, depends linearly of the symmetrized coordinates of nuclear vibrations Q, $E^{(1)}(Q) = F_I Q_I$.

If we consider now the second term of Equation 3.4 we can obtain the quadratic vibronic constants that are given by

$$W_{ij}^{(2)} = \frac{1}{2}\left\langle \psi_i^{(0)} \left| \left(\frac{\partial^2 V}{\partial Q_I \partial Q_J} \right) \right| \psi_j^{(0)} \right\rangle = F_{IJ} \tag{3.7}$$

The second order correction to the energy $E^{(2)}(Q)$ depends on the product $Q_I Q_J$.

Assuming that $\psi_i^{(0)} \in \Gamma_i$ and $\psi_j^{(0)} \in \Gamma_j$, linear vibronic constants $F_I \neq 0$ if $Q_I \in \Gamma_i \otimes \Gamma_j$ while quadratic vibronic constants $F_{IJ} \neq 0$ if $Q_I Q_J \in \Gamma_i \otimes \Gamma_j$. At this stage, vibronic couplings can be classified into three main categories, taking into account symmetry and degeneracy considerations of electronic states ψ_i and vibrational modes Q_I:

1. Totally symmetric combinations with vibrations Q_I belonging to irrep A_1. The distortion produced by nuclear displacements does not reduce the symmetry of the parent phase. The main contributions comes from the first order correction to the energy $E^{(1)}(Q)$. In this case, linear vibronic constants $F_I \neq 0$ for both degenerate and non-degenerate electronic states.

2. Vibronic combinations with modes Q_I where the electronic states ψ_i are degenerated and the first order correction $E^{(1)}(Q)$ is the main responsible of the distortion of the parent phase. The number of linear vibronic constants depends on the symmetry of the system. In this case, the vibronic coupling is associated with the Jahn-Teller (JT) effect, which is a first order effect.

3. Vibronic combinations with modes Q_I where the main coupling is between electronic states separated by an energy gap so the second order correction to the energy $E^{(2)}(Q)$ produces the most significant distortion. This is the so-called pseudo Jahn-Teller (PJT) effect, a second order perturbation effect.

It is worth noting that the three types of vibronic couplings are not mutually exclusive. Totally symmetric couplings (type 1) and PJT coupling (type 3) always appear whereas JT coupling requires spatially degenerated electronic states and, in this last case, there is a competition between PJT and JT effects, whose vibronic coupling intensities depend on the vibronic constants (Equations 3.6 and 3.4) leading the two effects to different physical consequences.

As explained in the following sections, JT and PJT effects can lead to distortions due to the vibronic coupling with modes Q_I which reduce the symmetry of the system. These distortions can be also understood in terms of the forces on ligand ions, which are associated with the difference between the real electron density and that coming from a closed shell ion with the same number of electrons [33].

The force induced on ligand k by the electron density can be written as follows [33]

$$\vec{F}(k) = \int \frac{n(\vec{r})(\vec{R}_k - \vec{r})}{|\vec{R}_k - \vec{r}|^3} q_L e^2 + \sum_{k \neq k} \frac{\vec{R}_k - \vec{R}_{k'}}{|\vec{R}_k - \vec{R}_{k'}|^3} q_L^2 e^2 - \frac{\vec{R}_k - \vec{R}_M}{|\vec{R}_k - \vec{R}_M|} q_M q_L e^2 \tag{3.8}$$

where $q_L e$ is the ligand charge and $q_M e$ the metal charge. The first term is the repulsive contribution due to electron density, the second is the repulsion with other ligands and the last one is the attraction with the metal nucleus.

For closed shell ions, this force is $\vec{F}(k) = 0$, since the associated electron density is totally symmetric. When the closed shell ion is replaced by an open shell ion, there is a change

in the electron density Δn, which is now asymmetric. This change in the density is the responsible of the net force exerted over the ligands and the following distortion. Hence, the fundamental theorem of DFT (Section 2.2) implies that variations in the electron density will lead to changes in the external potential and therefore in the geometry of the system [33].

3.2. E ⊗ e Jahn-Teller effect

The JT effect is a particular case of vibronic coupling, in which the predominant coupling is between *stricly degenerate* electronic states through a vibrational mode that reduces the symmetry of the parent phase.

The problem explained in this section is a simplification of the JT effect in AgF_2, where the ground state of AgF_6^{4-} units is characterized by two pairs of wavefunctions belonging to irrep E_g (see Section 4.2). In this case, the complex belongs to irrep D_{3d}, displaying trigonal symmetry. However, the distortions observed in the complexes are similar to those found in a triangular triatomic X_3 molecule with a 3-fold axis, where there are twofold degenerate E electronic states. In this system, the vibrational modes that provide vibronic constants (Equation 3.6) different from zero are the totally symmetric mode Q_a and E-type modes Q_x and Q_y [32], represented in Figure 3.1

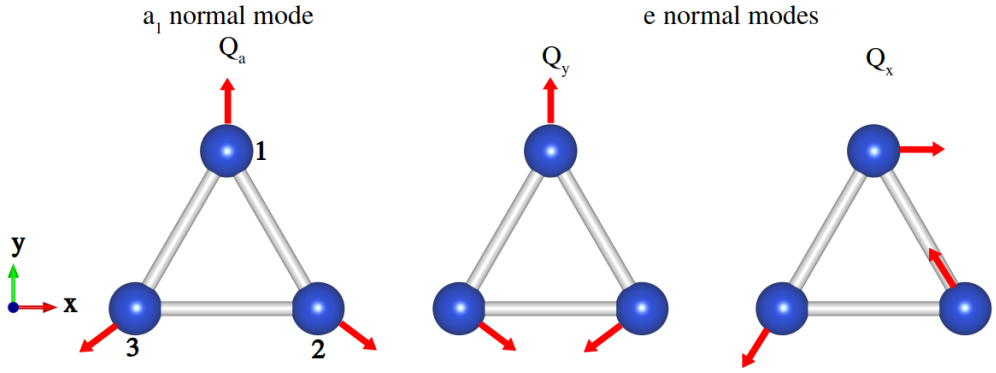

Figure 3.1: Symmetrized distortions in a triatomic triangular molecule X_3. Left: totally symmetric a_1 displacement that does not produce a symmetry breaking $Q_a = \frac{1}{\sqrt{12}}(2y_1+\sqrt{3}x_2-y_2-\sqrt{3}x_3-y_3)$. Center-right: doubly degenerate e displacements $Q_y = \frac{1}{\sqrt{12}}(2y_1 - \sqrt{3}x_2 - y_2 + \sqrt{3}x_3 - y_3)$ and $Q_x = \frac{1}{\sqrt{12}}(2x_1 - x_2 + \sqrt{3}y_2 - x_3 - \sqrt{3}y_3)$.

If we only take into account the linear vibronic coupling (Equation 3.6) and the quadratic elastic term, i.e., the term associated with linear combinations of the totally symmetric mode, the effective vibronic Hamiltonian is given by [34]

$$W(Q_x, Q_y) = E_0 + \frac{1}{2}K^{(0)}(Q_x^2 + Q_y^2)\sigma_z + F_I(Q_x\sigma_z - Q_y\sigma_x) \tag{3.9}$$

where $K^{(0)}$ is the primary force constante and σ_z and σ_x are the Pauli matrices

$$\sigma_z = \begin{pmatrix} 1 & 0 \\ 0 & -1 \end{pmatrix}, \sigma_x = \begin{pmatrix} 0 & 1 \\ 1 & 0 \end{pmatrix} \tag{3.10}$$

the diagonalization of the effective vibronic Hamiltonian gives rise to an APES of Mexican-hat-type (see Figure 3.2, left), whose energy in polar coordinates is given by [32]

$$E(\rho) = \frac{1}{2}K^{(0)}\rho^2 + F_I\rho \tag{3.11}$$

This APES is characterized by a conical intersection at $Q_I = 0$, which represents the high-symmetry configuration, where the three ions form an equilateral triangle. Within harmonic approximation and considering the linear vibronic constant, the points in the APES with the same ρ have the same adiabatic energy. Therefore, at minimum energy configuration we find a circumference of equivalent adiabatic minima with an energy that is related with the linear vibronic constant by [32]

$$E_{JT} = -\frac{F_I^2}{2K^{(0)}} \tag{3.12}$$

This is the JT stabilization energy, i.e., the energy gained after the distortion from the high-symmetry phase to the flattened isosceles triangle. The distortion is produced through the coupling between the doubly degenerate electronic state E with vibrational modes Q_x and Q_y represented in Figure 3.1.

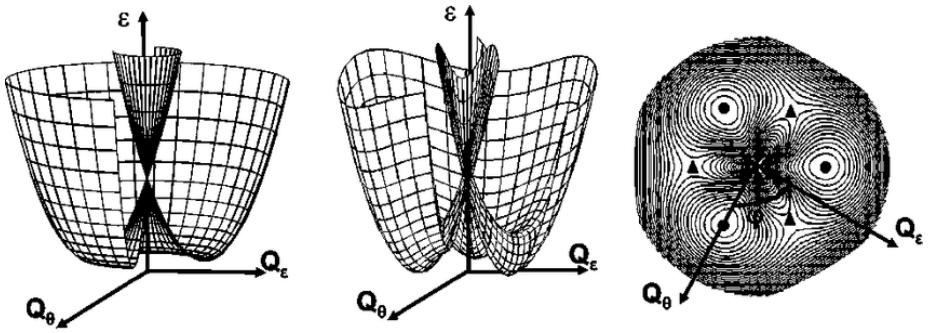

Figure 3.2: Adiabatic potential energy surface in JT effect. Left: Mexican hat potential. Center: warping of the Mexican hat where higher order energy terms are included. Right: top view of the warping, identifying three minima (circles) and saddle points (triangles). Reprinted from [35]

If higher order terms are include in the effective Hamiltonian, a warping of the Mexican hat potential is produced (Figure 3.2, center). In general, the cubic anharmonicity is the main contribution to the warping, while the coupling with higher energy states (PJT mixing terms) and quadratic vibronic coupling are less significant [35].

The warping of the APES implies the emergence of three equivalent minima (Figure 3.2, right) separated by three saddle points. In this conditions, there is an energy difference between the minima and the transition state, called the barrier B, whose value usually lies in the range 10-100 meV, one order of magnitude smaller than the JT stabilization energy [36]

The three adiabatic minima in the APES of JT problems are, in principle, equivalent. However, random strains present in crystals slightly stabilize one of these minima. Therefore, different centers can be distorted along different directions. At sufficiently low temperatures, the system can be locked in one of the minima, which is known as static JT effect. On the other hand, it could be observed a dynamic JT effect due to thermal fluctuations (incoherent) as well as to tunneling (coherent) [35].

Systems with 3-fold symmetry axes and more than three atoms have the same E terms as X_3 molecules. Among these materials is AgF_2, which has been studied in this work.

In this sort of systems, the JT problem is also E⊗e, but the quantitative analysis is complicated due to the presence of more e-type vibrations. This constitutes a multimode JT problem [37], as we will see in Section 3.4.

3.3. Pseudo Jahn-Teller effect

If JT effect is the dominant contribution to vibronic coupling, PJT effect participates in the warping of the Mexican hat potential. It is the responsible of vibronic mixing between the ground state and higher energy excited states [35].

By contrast to JT effect, where the coupling is produced at first perturbation order, PJT effect is a second order term. It couples two electronic states ψ_i and ψ_j, separated by an energy gap $E_i - E_j = 2\Delta$, through a vibrational mode Q_I. In this case, there are no constraints on the degeneracy of the electronic states.

In a simplified model, we assume only one vibrational mode Q_I that couples two electronic states ψ_i and ψ_j, whose APES have the same curvature and thus the same primary force constant $K^{(0)}$. The effective vibronic Hamiltonian can be written as follows

$$W(Q_I) = \frac{1}{2}K^{(0)}Q_I^2\mathbf{I} + F_I Q_I \mathbf{U}, \quad \mathbf{U} = \begin{pmatrix} 0 & 1 \\ 1 & 0 \end{pmatrix} \tag{3.13}$$

In order to obtain the energy of states ψ_i and ψ_j after the coupling through vibration Q_I, the vibronic Hamiltonian is diagonalized. The eigenvalues are the energies of the electronic states [32]

$$E_\pm = \frac{1}{2}K^{(0)}Q^2 \pm \Delta\sqrt{1 + \left(\frac{F_I Q}{\Delta}\right)^2} \tag{3.14}$$

where E_+ is the energy of the excited state ψ_j and E_- the energy of the ground state ψ_i after considering the vibronic coupling. The second term of Equation 3.14 can be expanded in Taylor series, considering that nuclear vibrations Q_I are small

$$E_\pm = \frac{1}{2}\left(K^{(0)} \pm \frac{F_I^2}{\Delta}\right)Q_I^2 \pm \Delta \pm ... \tag{3.15}$$

Considering the Taylor expansion of Equation 3.15 the force constant of the electronic states is $K_\pm = K^{(0)} \pm \frac{F_I^2}{\Delta} = K^{(0)} \pm K^\nu$, where $K^{(0)}$ is the same for both electronic states within this simplified model

$$K^{(0)} = \left\langle \psi_i^{(0)} \left| \frac{\partial^2 V}{\partial Q_I^2} \right| \psi_i^{(0)} \right\rangle \tag{3.16}$$

$K^{(0)}$ comes from the totally symmetric combinations of the quadratic vibronic constant (Equation 3.7) and accounts the contributions to the total force constant K with frozen electron density. On the other hand, the vibronic force constant K^ν comes from the linear vibronic coupling (Equation 3.6) and it includes contributions that depend on changes in the electron density due to the mixing of states separated by an energy gap 2Δ, as indicated in Equation 3.17

$$K^\nu = \frac{F_I^2}{\Delta} = \frac{1}{\Delta}\left|\left\langle \psi_i^{(0)} \left| \frac{\partial V}{\partial Q_I} \right| \psi_j^{(0)} \right\rangle\right|^2 \tag{3.17}$$

The instability theorem stated by Bersuker [32] claims that the primary force constant $K^{(0)} > 0$. Then, in the excited state ψ_j, $K > 0$ and therefore it is stable. However, it should be noted that the demonstration of this theorem involves the frozen orbitals approach throughout the distortion.

On the other hand, in the ground state, there is an energy decrease coming from the vibronic force constant K^{ν}, which is a possible source of instability. Therefore, we should analyse the value of the total force constant K. There are two possible situations:

1. $K^{(0)} > |K^{\nu}|$, which implies $K > 0$ (weak PJT effect): the curvature of the APES is decreased but the minimum remains at $Q_I = 0$. The symmetry of the system is not reduced (see Figure 3.3, left).
2. $K^{(0)} < |K^{\nu}|$, so $K < 0$ (strong PJT effect): the sign of the curvature becomes negative so there is an instability at $Q_I = 0$. The system undergoes an spontaneous symmetry breaking (see Figure 3.3, right). In general, in this case, the value of energy gap 2Δ is small, but it is not an essential condition since the value of K^{ν} also depends of the intensity of the vibronic coupling, characterized by the linear vibronic coupling F_I.

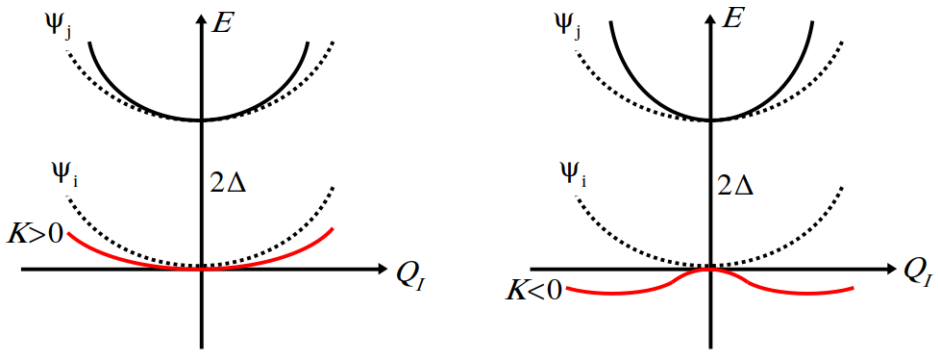

Figure 3.3: Changes in electronic states ψ_i and ψ_j from the parent phase (dotted line) when $K < 0$, (weak PJT effect, left) and $K > 0$ (strong PJT effect, right)

The coupling between the states ψ_i and ψ_j separated by an energy gap 2Δ through vibrational mode Q_I changes the wave functions of the electronic states and, therefore, the covalence of the bonding. By contrast, JT effect is driven by the forces of frozen electron density of degenerate states over ligand ions (Section 3.2). As mentioned at the beginning of this section, in this case, the changes in electron density due to PJT effect contributes to the warping of the Mexican hat [33].

3.4. Cooperative JT effect and magnetic order

In impurified systems where intercenter distances are small enough to observe interactions among impurities, the number of JT active modes involved in the vibronic coupling is very large. In these systems, the JT effect is a multimode problem. The limit case is found in periodic solids where the number of JT centers occupying regular lattice sites is infinite.

The multimode problem is important in the study of polyatomic molecules and especially in crystals where one cannot isolate one JT center from the rest of the lattice. These

problems are complicated since the number of vibrational modes as well as the number of vibronic constants increases with the size of the coordination sphere around the JT center [32].

For this reason, multimode solutions are complex and usually require some knowledge about the phonon spectrum of the crystal [32]. In these problems, analyses from first-principles calculations allow us to study cooperative effects in solids, which is a key element in this work.

Cooperative JT effects play an important role largely determining not only the structural properties of systems, but also the magnetic properties. In these systems, in addition to the ground state orbital degeneracy, there is also a Kramers (spin) degeneracy of the magnetic ions in the parent phase [21].

Determining the microscopic origin of magnetism is complicated since there are several mechanisms with similar energies, so the difference can be very slight. Magnetic interactions are characterized by two main features: open shell ions with magnetic moments different from zero and some covalent character in the bonding, so delocalization allows the overlap between electron clouds. Indeed, electrostatic interactions between electrons and nuclei are the main cause of magnetism [23]. Spin-orbit coupling and magnetic dipolar interactions are also involved in magnetism, as second order contributions.

Despite the microscopic origin of magnetism is known, qualitative and quantitative analysis of real systems is complicated due to the large number of interactions between electrons of different atoms, with different degrees of localization and energies. Furthermore, electron repulsions and spin orientations are correlated due to exchange interaction that comes from Pauli exclusion principle. On the other hand, electron-electron repulsions are connected with the rest of Coulomb interactions. Chemical bonding is under current study, especially in systems with small bond energies. The analysis of magnetism is even more complicated since it is driven by the bonding effect on spins orientations, which typically involves lower energies.

The study of magnetism is beyond one-electron approaches and, therefore, electron-electron interactions must be taken into account, particularly the exchange interaction. A thorough analysis of electronic respulsion is usually required and, besides the effect of electrons, the influence of nuclei should be included. In solids, this is very complex due to the large amount of particles and cooperative effects.

In this work we are focused on insulator magnetic materials, in which open shell magnetic ions (M = Cu^{2+}, Ag^{2+}) are separated by a non-magnetic ion (L = F^{-}, O^{2-}) as represented in Figures 1.1 and 1.3. In such cases, direct interaction among magnetic ions is small and the main mechanism of interaction is indirect and driven by the closed shell ion. This is the so-called superexchange interaction, where d-shell electrons of the metal polarized p-shell electrons of ligands, giving rise to magnetic coupling. Generally, in this type of systems, AFM coupling stabilizes. However, the energy difference between FM and AFM states is usually small ($\sim$ meV). This can be understood in the framework of the Heisenberg model of interacting spins, where the effective exchange Hamiltonian can be written as follows [21]

$$H_{\text{Heis}} = \frac{2t^2}{U} \sum_{\langle i,j \rangle} \vec{S}_i \vec{S}_j \tag{3.18}$$

where i and j indicate a summation over the nearest neighbors and $\vec{S}$ represents the spin. In Equation 3.18 there are two factors: the effective transition integral t which accounts electron hopping between different lattice sites and the Coulomb repulsion at one center U (on-site interaction). In non-degenerate states within a two electron approach, there is an energy gain in AFM configuration $\Delta E_{\mathrm{AFM}} = -\frac{2t^2}{U}$ with respect to FM configuration $\Delta E_{\mathrm{FM}} = 0$, since the hopping is forbidden by Pauli principle and thus $t = 0$. Furthermore, in magnetic insulators $t << U$, which explained the small energy difference between FM and AFM states. In many electron systems this scheme is noticeably more complicated, but the basic idea, in general, remains valid.

Between magnetic and non-magnetic insulator solids there are some differences that can be highlighted. The structure of the former is usually distorted, they often show structural phase transitions and the magnetic structure is quite complicated in most cases, displaying magnetic anisotropy and magnetostriction. It is worth noting that in solids containing these transition-metal ions, especially with E_g degeneracy, the relation between orbital and magnetic ordering is complicated [21].

In magnetic insulators with high concentration of open shell ions, crystalline distortions are not independent. Lattice deformation causes a symmetry breaking which is accompanied by orbital ordering. These two effects produce a modification of space-charge distribution [21].

4. Results: silver difluoride AgF_2

As explained in Section 1.2, the first material studied is AgF_2. In this chapter we have explored its structure and magnetism, starting from the parent phase and analysing how it is distorted into the experimentally observed one. In this analysis we have found that, despite the local symmetry of AgF_6^{4-} units involved in the parent phase is trigonal D_{3d}, there is a JT effect which causes a cooperative distortion, which leads to geometrical and magnetic layering. Following this line, our results show that the magnetic order in AgF_2 is determined by the vibronic contributions involved in JT effect.

4.1. Parent phase: structure and ground state

At ambient pressure and temperature, AgF_2 is a low symmetry compound, which belongs to the orthorhombic space group Pbca, as indicated in Figure 1.1. The local geometry of AgF_6^{4-} complexes within AgF_2 lattice is that of a distorted octahedron where the Ag^{2+}-F^- distances along the local directions $\vec{x}$, $\vec{y}$ and $\vec{z}$ are R_x = 2.074 Å, R_y = 2.067 Å and R_z = 2.584 Å [13]. It should be noted that, even though the distances in **xy** plane are quite close, the local symmetry is neither tetragonal D_{4h} nor orthorhombic D_{2h} since the angles $\widehat{FAgF}$ are different from 90^o. The calculated distances in AgF_6^{4-} units and cell parameters of AgF_2 lattice are gathered in Table 4.1, as well as the corresponding experimental values. There are slight variations from experiment to our simulations of less than 2%.

	a (Å)	b (Å)	c (Å)	R_x (Å)	R_y (Å)	R_z (Å)
Experimental	5.073	5.529	5.813	2.067	2.074	2.584
Calculated	5.178	5.622	5.766	2.094	2.096	2.618

Table 4.1: Experimental [13] and calculated values of cell parameters and Ag^{2+}-F^- bond lengths in AgF_2.

As explained in Section 1.1, the first step in our analysis is optimizing the reference structure of this system. In order to explore the ground state of the parent phase, as shown in Section 3.1, the asymmetric density produced by an open shell transition-metal ion M (M = Ag^{2+}) should be replaced by a symmetric density. This replacement allows us to examinate the structure of the system before considering the vibronic coupling and thus, in the absence of distortions.

By periodic simulations with Crystal code, all Ag^{2+} cations have been replaced by the closed shell $4d^{10}$ Cd^{2+} ions, whose ionic radii are quite similar (in sixfold coordinated complexes $R(Ag^{2+})$ = 1.01 Å, $R(Cd^{2+})$ = 1.09 Å) [38]. An advantage of Crystal over other first-principles codes is that it enables optimizing the geometry of the system within a determinated space group, which prevents a reduction of the symmetry.

After the substitution of Ag^{2+} by Cd^{2+} ions, both cell parameters and atomic positions have been relaxed. As a consequence, the system undergoes a spontaneous transition to the cubic phase $Pa\bar{3}$, depicted in Figure 4.1, which is, indeed, the parent phase of AgF_2.

At normal conditions, the most stable phase of CdF_2 is found for the flourite structure, shown in Figure 4.2. In this phase the symmetry of the compound is higher since it belongs to cubic space group $Fm\bar{3}m$, where Cd^{2+} cations are eightfold coordinated by F^- anions.

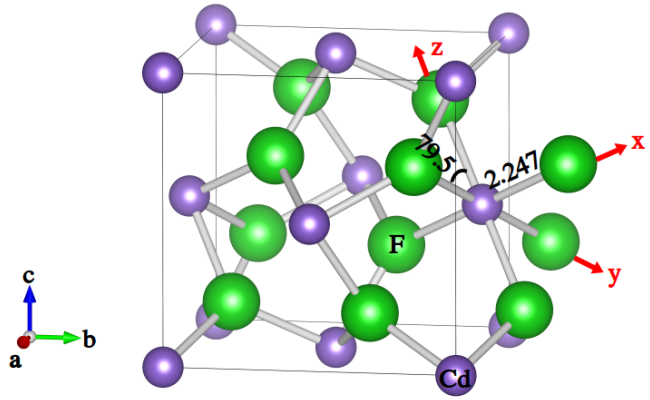

Figure 4.1: Parent phase of AgF_2, which belongs to the cubic $Pa\bar{3}$ space group. It was obtained by replacing the four Ag^{2+} ions in the unit cell by Cd^{2+} ions. Metal-ligand distances and one $\widehat{FCdF}$ angle are indicated in a single CdF_6^{4-} complex. The optimized lattice vector is $a = 5.497$ Å.

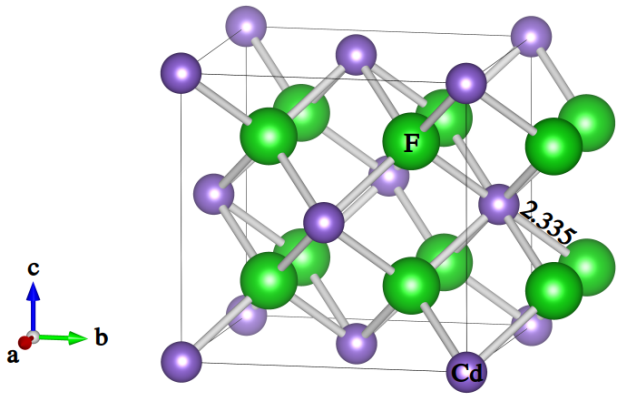

Figure 4.2: Fluorite structure of CdF_2 of cubic $Fm\bar{3}m$ space group (lowest energy configuration). The distance between Cd^{2+} and F^- is indicated on CdF_8^{6-} complex. The lattice vector is $a = 5.393$ Å.

If we compare flourite structure of CdF_2 (Figure 4.2) with the optimized $Pa\bar{3}$ displayed in Figure 4.1, both structures are rather similar. However, the coordination of Cd^{2+} cations changes from eightfold to sixfold when the symmetry of the compound is reduced from $Fm\bar{3}m$ to $Pa\bar{3}$. Taking this fact into account, there are two Cd^{2+}-F^- bonds that were broken, reinforcing the other six bonds. Hence, metal-ligand distances in fluorite structure are greater (2.335 Å) than in $Pa\bar{3}$ phase (2.247 Å). On the other hand, the distance from Ag^{2+} ion to the next closest F^- ion in $Pa\bar{3}$ is 3.096 Å, reflecting the bond breaking.

At this point, we will focus on the ground state of a single AgF_6^{4-} complex in $Pa\bar{3}$ phase of AgF_2. Although metal-ligand distances are identical in this structure, the angles are not equal to 90^o (Figure 4.1) and therefore the local symmetry is not octahedral O_h but trigonal D_{3d}. It is worth noting that the ground state of a single AgF_6^{4-} complex when one Cd^{2+} ion is replaced by Ag^{2+}, keeping cubic $Pa\bar{3}$ structure, is orbitally twofold degenerate. This result was obtained through cluster calculations on isolated AgF_6^{4-} complex as well as embedded in CdF_2 lattice, i.e., including the electrostatic potential V_R.

In Table 4.2 the energies of each molecular orbital in the complex (ε) as well as its charge distribution calculated by means of Mulliken population analysis are collected. In order to simulate the complex in the parent phase we have used the initial electronic configuration $(3z^2 - r^2)^{1.5}(x^2 - y^2)^{1.5}$. This unreal configuration enable us to reproduce the behaviour of a closed shell ion, where the electron density is symmetric.

	In vacuo		$+V_R$	
Occupation	ε (eV)	Mulliken population	ε (eV)	Mulliken population
1.5	12.788	50% x^2-y^2 + 3% z^2 + 3% xz + 2% yz	-6.549	56% x^2-y^2 + 3% xz + 2% z^2 + 2% yz
1.5	12.787	54% z^2 + 2% x^2-y^2 + 1% xy + 1% yz	-6.549	58% z^2 + 2% x^2-y^2 + 1% yz
2.0	10.894	37% xz + 16% yz + 5% x^2-y^2 + 2% xy	-8.446	41% xz + 19% yz + 6% x^2-y^2 + 2% xy
2.0	10.894	29% xy + 26% yz + 6% xz	-8.446	33% xy + 28% yz + 7% xz
2.0	10.832	28% xy + 15% yz + 14% xz + 2% z^2	-8.508	36% xy + 19% yz + 18% xz + 3% z^2

Table 4.2: Orbital energies, ε, and Mulliken charge distributions in AgF_6^{4-} complex at the optimized geometry of the parent phase of AgF_2, that is the $Pa\bar{3}$ CdF_2 structure. Calculations have been carried out for an isolated complex and also considering the embedding through the electrostatic potential V_R due to the rest of ions of the crystal. The electronic configuration is such that the electrons in the d-shell are uniformly distributed between x^2-y^2 and $3z^2-r^2$ orbitals.

Considering the previous results, we have proved that the ground state of AgF_6^{4-} remains twofold degenerate (E_g) when the local symmetry is reduced from octahedral O_h to trigonal D_{3d}. Therefore, the conditions of symmetry and orbital degeneracy in the parent phase $Pa\bar{3}$ are compatible with JT effect, which breaks the symmetry and lifts the degeneracy, stabilizing the orthorhombic Pbca phase. In the next section we will discuss how the cooperative trigonal distortion leads the system to the experimental structure of AgF_2.

4.2. Trigonal distortion

Since the ground state of AgF_2 remains doubly degenerate under the symmetry descent from O_h to D_{3d} the system can experience a JT effect under trigonal symmetry. Additionally, this effect in AgF_2 is actually a multimode problem, involving atomic positions (local distortion) as well as cell parameters (lattice distortion).

As indicated in Table 4.2, under D_{3d} symmetry there are two pairs of wavefunctions of $4d^9$ orbitals of Ag^{2+} which belong to irrep E_g (x^2-y^2, xy) and (xz, yz), where {X, Y, Z} are the basis in trigonal coordinates (Figure 4.3). Furthermore, in trigonal symmetry, the three adiabatic minima characteristic of JT effect do not show tetragonal symmetry as it occurs when the parent phase is octahedral.

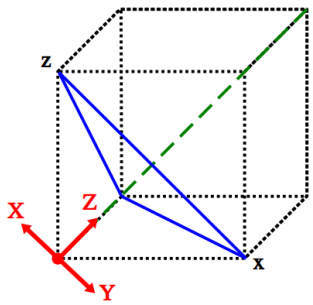

Figure 4.3: Basis of trigonal coordinates {X, Y, Z} (red). In cartesian coordinates (black) the vectors along X, Y and Z directions can be written as X(-1/$\sqrt{6}$, -1/$\sqrt{6}$, 2/$\sqrt{6}$), Y(1/$\sqrt{2}$, -1/$\sqrt{2}$,0) and Z(1/$\sqrt{3}$, 1/$\sqrt{3}$, 1/$\sqrt{3}$).

When one of Cd^{2+} ions in $Pa\bar{3}$ structure of CdF_2 is replaced by Ag^{2+}, an unstable vibrational mode of frecuency $\omega = 138i$ distorts the system, as represented in Figure 4.4. Metal-ligand distances obtained by the optimization of atomic positions in the lattice after the $Cd^{2+} \rightarrow Ag^{2+}$ substitution are collected in Table 4.3.

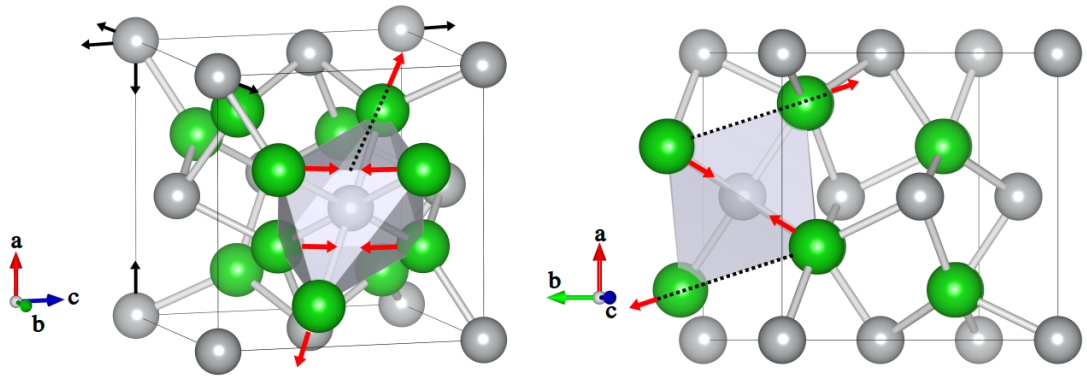

Figure 4.4: Distortion of AgF_6^{4-} complex (red arrows) and lattice vectors (black arrows) in cubic $Pa\bar{3}$ phase of AgF_2. Under this distortion the equilateral triangles defined by three F^- ions are flattened into acute triangles in orthorhombic Pbca phase. Lattice vectors are elongated in two directions (b and c) and compressed in the third one (a).

System	R_x (Å)	R_y (Å)	R_z (Å)
CdF_2:Ag^{2+} (1)	2.128	2.134	2.445
CdF_2:Ag^{2+} (3)	2.077	2.146	2.532
AgF_2	2.067	2.074	2.584

Table 4.3: Ag^{2+}-F^- distances in CdF_2 lattice with a single Ag^{2+} impurity per unit cell (first line), three Ag^{2+} impurities per unit cell (second line) and pure AgF_2. The local coordinates x, y and z are the ones indicated in Figure 4.1.

The presence of Ag^{2+} impurities in CdF_2 lattice induces the trigonal distortion displayed in Figure 4.4, which flattened the trigonal complex, lifting the degeneracy of the ground state in $Pa\bar{3}$ structure (Table 4.2). As shown in Figure 4.4 this deformation is significantly different from the usual tetragonal one. In contrast to what is found for an initial octahedral complex, where the tetragonal distortion is produced along bond axes, in a trigonal complex the distortion is such that elongates the initial equilateral triangles in $Pa\bar{3}$ phase into acute ones in orthorhombic Pbca structure.

As gathered in Table 4.3, there is a relation between the concentration of Ag^{2+} ions in CdF_2 lattice and the deformation of the structure. Metal-ligand distances in CdF_2:Ag^{2+} get closer to those found in pure AgF_2 as the silver content in CdF_2 lattice increases. In the next section we have calculated the potential energy surfaces associated with the distortion produced by both atomic coordinates and lattice parameters, as well as the effect of this deformation in the magnetic order of the system.

4.3. Jahn-Teller effect and magnetism

As shown in Section 4.1, in the high-symmetry phase $Pa\bar{3}$ of AgF_2 the ground state is twofold degenerate and hence, the system is distorted into orthorhombic Pbca structure due to the existence of cooperative Jahn-Teller effect. One of the main features of this effect is the presence of two distortions whose energies are close but differ by a small energy barrier, B, which is usually in the range of 10-100 meV [36].

In order to determine the barrier B and the stabilization energy E_{JT} we have analysed the potential energy surface with the cooperative JT deformation. To obtain the potential energy surface we have built a linear transformation of both atomic coordinates and lattice parameters that enables us to interpolate between the cubic phase $Pa\bar{3}$ and the orthorhombic phase Pbca.

The problem is different when the high-symmetry phase is octahedral, for example, in d^9 doped systems with rock salt structure (NaF:Ag^{2+}, NaCl:Ag^{2+}), where the impurity occupies an atomic site with O_h symmetry. Then, the JT effect produces an elongated tetragonal distortion until the system reaches one of the three adiabatic minima of the potential energy surface. In this sort of systems, our periodic calculations allow us to stabilize the saddle point (compressed octahedron) due to symmetry constraints. If the symmetry of the transition state is D_{4h}, the calculation is carried out within that symmetry so the orthorhombic vibrational modes that could distort the system from compressed to elongated octahedron (minimum energy configuration) are not accesible and therefore, we can optimize the geometry of the system in the saddle point.

In these d^9 doped systems we can described the tetragonal distortion using a single parameter, η, which can be written as follows

$$\begin{aligned} R_z &= \langle R \rangle + 2\eta \\ R_x = R_y &= \langle R \rangle - \eta \end{aligned} \tag{4.1}$$

where $\langle R \rangle$ is the metal-ligand distance in octahedral symmetry. Although in AgF_2 the distortion is driven by the change in both atomic coordinates and lattice vectors, regarding a *single* AgF_6^{4-} complex we can describe the deformation in terms of a tetragonal distortion, characterized by η, such as in octahedral JT effect.

In AgF_2, the minimum and the transition state of the potential energy surface are calculated within orthorhombic Pbca group. Under these conditions, there are forces that change the geometry of AgF_6^{4-} complexes in the optimization of the saddle point, leading the system to the lowest energy configuration. In this case, the shape of the triangular faces defined by three fluorine ions turns from obtuse (Figure 4.5, $\eta = -0.10$) to acute triangles (Figure 4.5, $\eta = 0.16$). On this basis, we have built a linear transformation of both atomic positions and lattice parameters that allows us to interporlate between the high-symmetry phase $Pa\bar{3}$ ($\eta = 0.0$ in Figures 4.5, 4.6) and the minimum energy configuration in orthorhombic Pbca phase ($\eta = 0.16$ in Figures 4.5, 4.6) as well as the saddle point of the potential energy surface ($\eta = -0.10$ in Figures 4.5, 4.6). Then, the stabilization energy E_{JT} and the barrier B can be estimated.

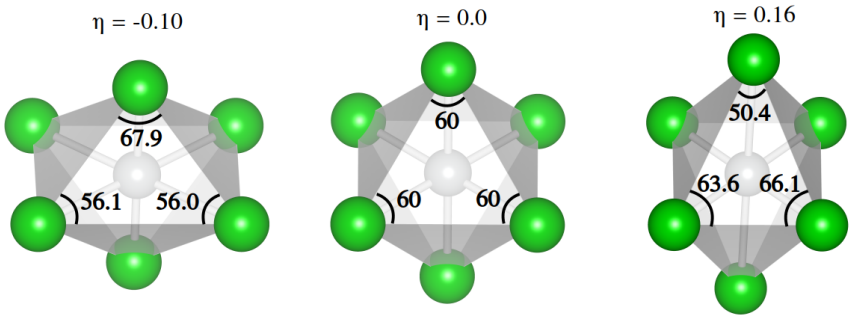

Figure 4.5: AgF_6^{4-} trigonal complexes in AgF_2 lattice at different points of potential energy surface: transition state $\eta = -0.10$, high symmetry configuration $\eta = 0.0$ and minimum $\eta = 0.16$.

Regarding the linear transformation of atomic coordinates, Ag^{2+} ions were keeping fixed in the unit cell whereas F^- ions were simultaneously displaced as shown in Figure 4.4, in order to cooperatively distort the four AgF_6^{4-} complexes. The atomic coordinates of fluorine atoms in AgF_2 lattice are modified as follows

$$\begin{aligned} X_{\mathrm{F}} &= 0.1748 + 0.0091363\lambda \\ Y_{\mathrm{F}} &= 0.1748 + 0.0194123\lambda \\ Z_{\mathrm{F}} &= 0.3252 + 0.0482214\lambda \end{aligned} \tag{4.2}$$

In Equation 4.2, parameter λ goes from -1.0 to 1.0 in steps of 0.1, where $\lambda = 0$ provides the geometry in the parent phase $Pa\bar{3}$.

Similarly, another linear transformation was used to calculate the modulus of unit cell vectors $\vec{a}$, $\vec{b}$ and $\vec{c}$ on each point of the potential energy surface. In this case, we have split the interpolation in the two branches ($\eta < 0$ in Equation 4.3 and $\eta > 0$ in Equation 4.4) since the relaxation of the lattice vectors is different on each case (see Figure 4.6, bottom).

$$\begin{aligned} a_{\eta<0} &= a_{\mathrm{Pa}\bar{3}} + 0.3633\lambda \\ b_{\eta<0} &= a_{\mathrm{Pa}\bar{3}} - 0.2950\lambda \\ c_{\eta<0} &= a_{\mathrm{Pa}\bar{3}} - 0.2083\lambda \end{aligned} \tag{4.3}$$

$$\begin{aligned} a_{\eta>0} &= a_{\mathrm{Pa}\bar{3}} - 0.4488\lambda \\ b_{\eta>0} &= a_{\mathrm{Pa}\bar{3}} + 0.0588\lambda \\ c_{\eta>0} &= a_{\mathrm{Pa}\bar{3}} + 0.4375\lambda \end{aligned} \tag{4.4}$$

In Equation 4.3, parameter λ goes from -1.0 to 0.0 while in Equation 4.4 goes from 0.0 to 1.0, in steps of 0.1, as mentioned above.

With these linear transformations of both atomic positions and cell parameter we can compute the energy curves of AgF_2, distorting from the parent $Pa\bar{3}$ phase the four AgF_6^{4-} units involved simultaneously (Figure 4.6, top). Lattice paramenters are also relaxed, (Equations 4.3 and 4.4) in order to reproduce the cooperative deformation of this system (Figure 4.6, bottom).

The distortion of lattice vectors from cubic $Pa\bar{3}$ phase at minimum energy configurations for each branch is collected in Table 4.4. For a single AgF_6^{4-} complex, the barrier B, which is the energy difference between the minima $\eta = 0.16$ and the transition state $\eta = -0.10$ and the stabilization energy E_{JT}, i.e., the energy gained with the distortion from the high-symmetry configuration ($\eta = 0.0$, see Figure 4.5) to the flattened trigonal complex ($\eta = 0.16$) are also included.

η (Å)	Energy (meV)	a (Å)	b (Å)	c (Å)
0.16	0	5.138	5.544	5.847
-0.10	88	5.715	5.320	5.372
0.0	193	5.497	5.497	5.497

Table 4.4: Lattice parameters a, b and c at each critical point of the potential energy surface. The results are given in terms of the local distortion η of a single AgF_6^{4-} complex.

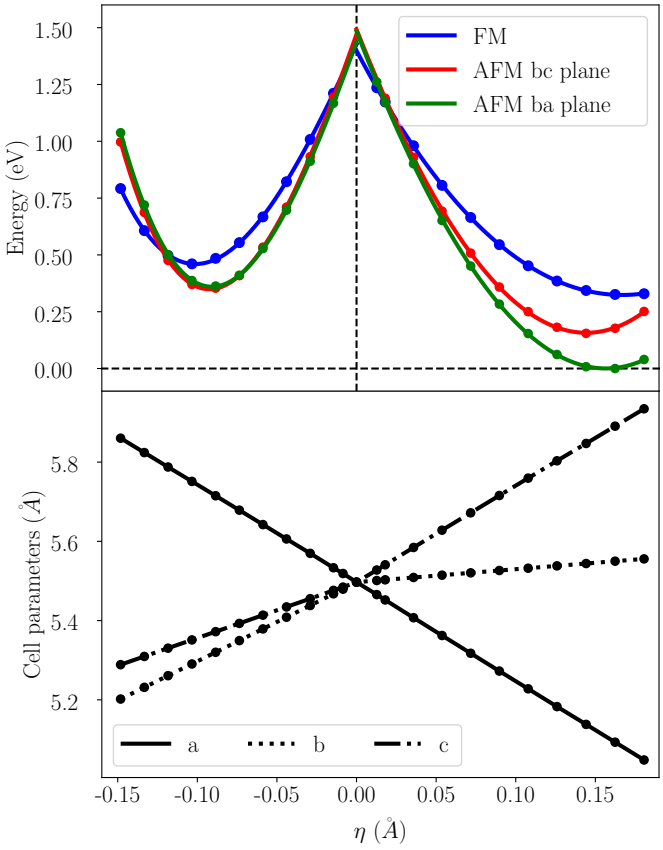

Figure 4.6: Top: energy of the unit cell when the four AgF_6^{4-} complexes involved in AgF_2 lattice are cooperatively distorted. Single point calculations with different arrangements of spins have been carried out: FM order (blue line), AFM in **bc** plane (red line) and AFM in **ba** plane (green line). Bottom: linear tranformation of lattice vectors a, b and c given in Equations 4.3 and 4.4.

The saddle point is found for the $\eta < 0$ branch at $\eta = -0.10$, 88 meV above the lowest energy configuration. As mentioned above, this is precisely the value of the energy barrier B in this system, which corresponds to one of the four AgF_6^{4-} complexes involved in the distortion. The value lies in the typical range found for other d^9 ions in cubic crystals [36].

As noted previously, in contrast to molecules or d^9 centers in pure crystals, in AgF_2, the cooperative JT effect is a multimode problem, since it is determined by two degrees of freedom, the deformation of AgF_6^{4-} units and the relaxation of lattice vectors. There is another variable that we have considered to obtain the results shown in Figure 4.6: the magnetic order. Regarding AFM configurations, we have calculated the energy curves for two arrangements of spins, which are represented in Figure 4.7. As shown in Figure 4.6, the magnetic state of the lowest energy configuration is different on each critical point (high symmetry phase, saddle point and minimum). In the minimum of $\eta > 0$ branch, the energy difference per formula unit between AFM magnetic configurations is 37 meV, less than the energy barrier. For the $\eta < 0$ branch this difference is one order of magnitude smaller. Therefore, it can be concluded that the magnetism of the ground state in AgF_2 could be controlled through the variation of lattice parameters, as occurs in ferroelastic materials. It can be noted that we are using an approximate model of magnetism, in which the spins are collinear, whereas in the real system the AFM order presents a non-collinear arrangement of spins.

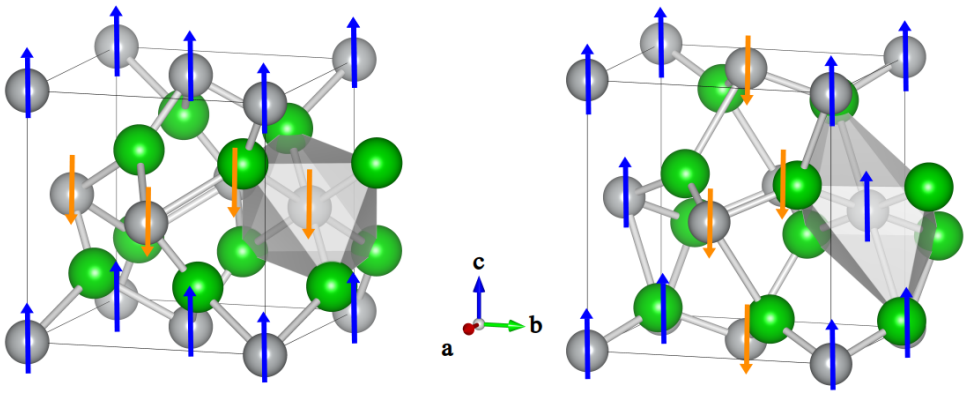

Figure 4.7: AFM orders in AgF_2 lattice employed in the calculations. Left: AFM in **bc** plane, which provides the lowest energy at $\eta = -0.10$. Right: AFM in **ba** plane, which corresponds to the minimum energy configuration at $\eta = 0.16$.

4.4. Layered structure and ferroelasticity

As discussed in Section 4.1 the parent $Pa\bar{3}$ phase of AgF_2 is cubic, where the four AgF_6^{4-} complexes involved in the unit cell belong to D_{3d} symmetry point group. Thus, in the high-symmetry configuration, the Ag^{2+}-F^- bonds are equivalent. The results obtained by cluster calculations with ADF for a single AgF_6^{4-} unit, which are gathered in Table 4.2, indicate that the ground state of this system is twofold degenerate, in which four of the five $4d^9$ orbitals of Ag^{2+} cation belong to irrep E_g. In this conditions, the potential energy surface displays three minima. Since the high-symmetry situation is unstable due to orbital degeneracy, the system undergoes a phase transition to orthorhombic Pbca group. On all complexes, the local distortion is equivalent, the equilateral triangle formed by three flourine atoms is elongated into an acute one, along the Z axis in trigonal coordinates (Figures 4.3 and 4.4), resulting in a flattened trigonal complex (Figure 4.5 $\eta = 0.16$).

In contrast to molecules or d^9 doped systems with rock salt structure, where the complex deformation is local, in pure AgF_2 this distortion is a cooperative effect, followed by a lattice relaxation from cubic a = 5.497 Å in $Pa\bar{3}$ to a = 5.073 Å, b = 5.529 Å and c = 5.813 Å in Pbca. Hence, axis a is compressed while c is elongated, as represented in Figures 4.4 and 4.6 (bottom) for $\eta > 0$ branch. This distortion has lead to the usual interpretation of AgF_2 as a layered system in c axis, since in this direction the Ag^{2+}-F^- bonds are weaker than intra-layer bonds due to the JT distortion.

Our analysis of this structure is carried out from the point of view of symmetry, studying the distortion of the parent $Pa\bar{3}$ phase, which is cubic and therefore devoid of AgF_2 layers. From this perspective, we have seen that the potential energy surface has the properties expected in a JT effect, where there are three adiabatic minima so the system may evolve to any of them. In the light of these findings, we can conclude that, like other JT cooperative systems [39], AgF_2 is a ferroelastic material. The barrier per single AgF_6^{4-} complex is 88 meV so the other configurations could be reached by the application of mechanics efforts (pressure) or growing the material in determinated substrates.

Bearing these facts in mind, AgF_2 is fairly different from actual layered systems such as K_2CuF_4, Cs_2AgF_4 or La_2CuO_4, also studied in this work. In these systems the complexes MX_6 (M = Cu^{2+}, Ag^{2+}, X = F^-, O^{2-}) are independent on each MX_2 slab (see Figure 1.3), whereas in AgF_2 there are intra-layer and inter-layers bonds, which can be hardly

considered as located in a single layer. Furthermore, the high-symmetry phase of these layered perovskites is not cubic but tetragonal I4/mmm, devoids of orbital degeneracy and thus of JT effect. These differences can be observed through the bands diagrams of both type of systems. If we consider the dispersion along $\Gamma \rightarrow Z$ path, in layered perovskites the bands are essentially flat (see the band diagram for K_2CuF_4 in Figure 5.7) indicating that the interaction between two layers could be neglected. On the other hand, in AgF_2 the dispersion is similar in all directions explored in the reciprocal space, as shown in the band diagram displayed in Figure 4.8.

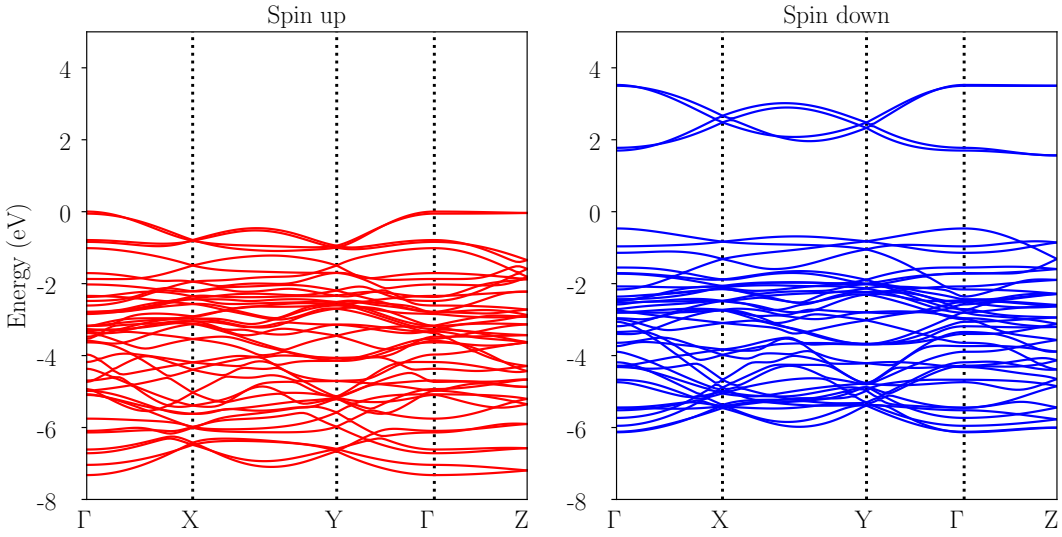

Figure 4.8: Band diagram of AgF_2 by spin channel calculated for both in plane ($\Gamma \rightarrow X \rightarrow Y \rightarrow \Gamma$) and out of plane ($\Gamma \rightarrow Z$) directions.

In Figure 4.8 we have represented the bands of FM state (which maximize dispersion) of pure AgF_2 by spin channel. If we consider the bands in the perpendicular direction near the Fermi energy, they are quite flat, while in the central zone there are dispersive bands and non-dispersive bands, which also happens in other directions. By contrast, in layered perovskites (Figure 5.7) even the more dispersive bands in $\Gamma \rightarrow Z$ direction are flatter than in AgF_2 in a smaller range of k space.

4.5. Magnetic order

Finally, some ideas about the magnetism in AgF_2 could be emphasized. First, in the cubic $Pa\bar{3}$ phase, AFM order is geometrically frustrated [40]. In this configuration ($\eta = 0$), the FM order is prefered instead of the AFM ones (Figure 4.6). Once the JT effect occurs and produces the distortion shown in Figure 4.4, elongating one lattice axis and compressing other, the frustration vanishes, giving rise to strong AFM coupling in **ba** plane and weak FM coupling in **bc** plane, result also provided by experimental measurements [41], which is consistent with the effect of superexchange interactions that usually lead to AFM coupling. Therefore, cooperative JT effect is a key element in the stabilization of the AFM state in AgF_2 system.

On the other hand, the results represented in Figure 4.6 show a change in the AFM order for the two branches. This variation is a consequence of the vibronic interactions existing in JT effect. The trigonal distortion of AgF_6^{4-} complexes to acute ($\eta > 0$) or obtuse ($\eta < 0$) triangles (Figure 4.5) as well as the switch of elongation axis of the AgF_2 lattice from c to a stabilizes two different AFM configurations.

5. Results: layered perovskites K_2CuF_4, Cs_2AgF_4 and La_2CuO_4

In Section 1 we have seen that cubic perovskite is the basis for other related structures such as layered perovskites, which have been studied in this work. Specifically, we have been focused on K_2CuF_4, Cs_2AgF_4 and La_2CuO_4, where MX_6 complexes (M = Cu^{2+}, Ag^{2+}, X = F^-, O^{2-}) are separated by slabs of rock salt structure AX (A = K^{2+}, Cs^{2+}, La^{3+}) (see Figure 1.3). As explained in Section 1.3, first- and second-principles calculations have been performed to analyse the change in the magnetism of these systems, with the ultimate goal of controlling the magnetic order of the ground state.

5.1. Low-symmetry and high-symmetry phases

The first step in the analysis carried out in this work was optimizing the geometry of the three layered systems K_2CuF_4, Cs_2AgF_4 and La_2CuO_4 in both the high-symmetry parent phase (tetragonal space group I4/mmm) and low-symmetry phase (orthorhombic Cmca). In Table 5.1 experimental and calculated values of lattice parameters and metal-ligand distances in MX_6 units are collected. All calculated values show great accordance with experimental findings, with slight variations within 2% error.

System	Magn.	Result	a (Å)	b (Å)	c (Å)	R_x (Å)	R_y (Å)	R_z (Å)
K_2CuF_4	FM	Exp. [42]	5.866	5.866	12.734	1.941	2.234	1.939
		Calc.	5.864	5.865	12.760	1.910	2.237	1.950
Cs_2AgF_4	FM	Exp. [6]	6.439	6.434	14.149	2.112	2.441	2.111
		Calc.	6.455	6.454	14.382	2.106	2.458	2.130
La_2CuO_4	AFM	Exp. [43]	5.402	5.361	13.155	1.905	1.905	2.413
		Calc.	5.456	5.305	12.943	1.907	1.907	2.404

Table 5.1: Experimental and calculated values of cell parameters and metal-ligand distances in the true low-symmetry phase Cmca of layered systems K_2CuF_4, Cs_2AgF_4 and La_2CuO_4. The calculated results correspond to the lowest energy magnetic order.

In these lattices, the local symmetry of MX_6 units is orthorhombic, with three different metal-ligand distances and angles $\widehat{XMX} = 90^o$, so the symmetry point group is D_{2h}. The complexes are elongated along local direction $\vec{y}$ in **ab** plane (see Table 5.1 and Figure 1.3).

Experimental geometries have been optimized for both FM and AFM orderings. The lowest energy magnetic state in these systems corresponds to the experimentally determined magnetic order. The energy differences between FM and AFM states are gathered in Table 5.3.

Regarding the high-symmetry phase, the three compounds comes from the same parent phase of K_2NiF_4-type structure, represented in Figure 5.1, where the main C_4 axis lies along cell vector $\vec{c}$. When the symmetry of this phase is reduced to the orthorhombic one, the two transition-metal ions in plane **ab** are not equivalent and the cell is doubled. In order to explore the parent phase, we have optimized within I4/mmm space group the three structures. Distances in the complexes and lattice parameters are gathered in Table 5.2.

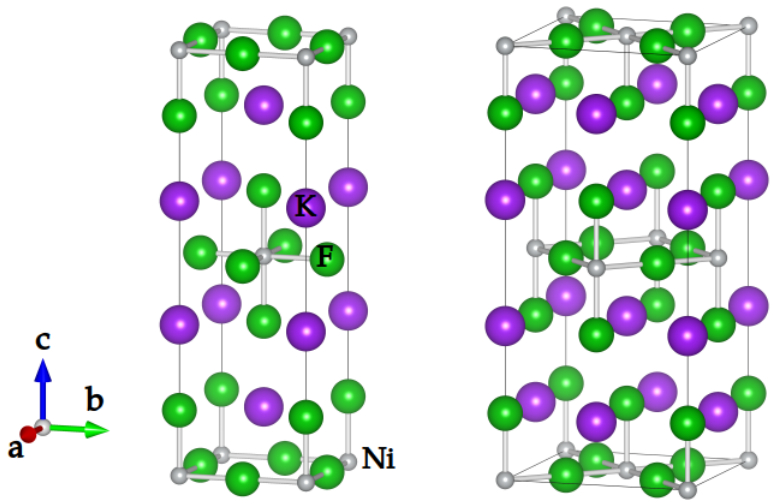

Figure 5.1: Left: K_2NiF_4 parent structure I4/mmm of K_2CuF_4, Cs_2AgF_4 and La_2CuO_4 lattices. Right: conventional cell expanded to $\sqrt{2} \times \sqrt{2} \times 1$ supercell

As for low-symmetry phase, geometry optimizations of the parent phase have been performed for both FM and AFM configurations. In order to accomodate both magnetic orders, the supercell represented in Figure 5.1 (right) has been employed. The results of these calculations show that the lowest energy is obtained for AFM state in all systems, as indicated in Table 5.2

System	Magn.	a (Å)	c (Å)	R_{eq} (4X) (Å)	R_{ax} (2X) (Å)
K_2CuF_4	AFM	4.155	12.637	2.078	1.912
Cs_2AgF_4	AFM	4.585	14.236	2.293	2.081
La_2CuO_4	AFM	5.334	13.009	1.886	2.389

Table 5.2: Calculated values of lattice parameters and metal-ligand distances in high-symmetry parent phase I4/mmm of layered perovskites K_2CuF_4, Cs_2AgF_4 and La_2CuO_4. The results correspond to the magnetic order of lowest energy.

As shown in Table 5.2, in high-symmetry phase, the local symmetry of MX_6 units is tetragonal D_{4h}. In K_2CuF_4 and Cs_2AgF_4 the complexes are compressed along $\vec{z}$ direction and the electron is localized in $x^2 - y^2$ orbital, whereas in La_2CuO_4 they are elongated in this direction, and the electron is localized in $3z^2 - r^2$ orbital.

If FM and AFM states for both phases are compared, the differences found in lattice parameters as well as in metal-ligand distances, whose values are ~ 0.01 Å, are negligible. The energy differences between the two magnetic configurations are quite small in the case of fluorine perovskites K_2CuF_4 and Cs_2AgF_4, but much larger for La_2CuO_4, as shown in Table 5.3.

System	ΔE_{HS} (meV)	ΔE_{LS} (meV)
K_2CuF_4	4.6	5.1
Cs_2AgF_4	7.9	11.4
La_2CuO_4	203.7	181.9

Table 5.3: Energy difference per formula unit between FM and AFM states in high-symmetry (HS) and low-symmetry (LS) phases of K_2CuF_4, Cs_2AgF_4 and La_2CuO_4 systems.

5.2. Magnetic order and PJT distortion

In geometry optimizations, the forces over a given nucleus are calculated with the potential energy gradient

$$\vec{F} = \langle \psi_0 | \vec{\nabla}_R V | \psi_0 \rangle \tag{5.1}$$

When the minimum energy configuration is reached, the forces are zero over each atom. In practical problems, if the force is below some threshold, it is assumed that the minimum of the APES is reached. If not, atoms are displaced and the forces are recomputed. In some first-principles software, as Crystal code, geometry optimizations incorporate the symmetry of the space group, so the internal coordinates are expressed in terms of the symmetry allowed deformations within the fixed space group [26]. Thus, nuclear coordinates can be written in terms of the vibrational modes Q.

In minimum energy configuration of the high-symmetry phase (space group I4/mmm) the forces are zero since the APES is quadratic close to $R = 0$. In order to relax the lattice, a distortion following an orthorhombic vibrational mode is performed, displacing simultaneously the equatorial ligands of the lattice as shown in Figure 5.2. This unstable mode, whose associated frequencies are gathered in Table 5.4, belong to irrep B_{1g} and it is found in both K_2CuF_4 and Cs_2AgF_4 parent phases.

System	Magn.	ω (cm^{-1})
K_2CuF_4	FM	$379.7i$
	AFM	$327.5i$
Cs_2AgF_4	FM	$281.3i$
	AFM	$242.8i$

Table 5.4: Frequencies of orthorhombic vibrational mode $Q_{b_{1g}}$ for both magnetic states.

As explained in Section 3.3 the force constant K becomes negative due to vibronic contribution K^ν (strong PJT effect) which leads to an spontaneous symmetry breaking. In this case, the symmetry of K_2CuF_4 and Cs_2AgF_4 is reduced from tetragonal I4/mmm to orthorhombic Cmca.

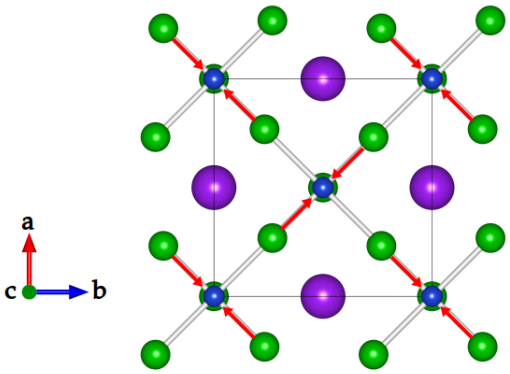

Figure 5.2: Orthorhombic distortion in **ab** plane produced by the displacement of equatorial ligands L = F^-, O^{2-}. Axial ligands remain fixed in the lattice throughout the distortion.

In order to determine the magnetic order of the systems as a function of the distortion coordinate, single point energy calculations for FM and AFM orders have been carried out.

In these calculations we started from the high-symmetry parent phase, in which the atomic position in the unit cell of equatorial ligand ions, that are those represented in Figure 5.2, is $\vec{R}_L = (0.25, 0.25, 0.0)$ in fractional units. The orthorhombic vibrational mode depicted in Figure 5.2 has been simulated through the displacement of these equatorial ligands in **ab** plane. The variation of atomic coordinates along the distortion, for the ligand at $\vec{R}_L$ is given by

$$\begin{aligned} X_L = Y_L &= 0.25 + \lambda \\ Z_L &= 0.0 \end{aligned} \tag{5.2}$$

where λ goes from 0 to 0.02 in steps of 0.001. The energy of both FM and AFM states has been calculated for each step of the distortions, as represented in Figures 5.3 (K_2CuF_4), 5.4 (Cs_2AgF_4) and 5.5 (La_2CuO_4).

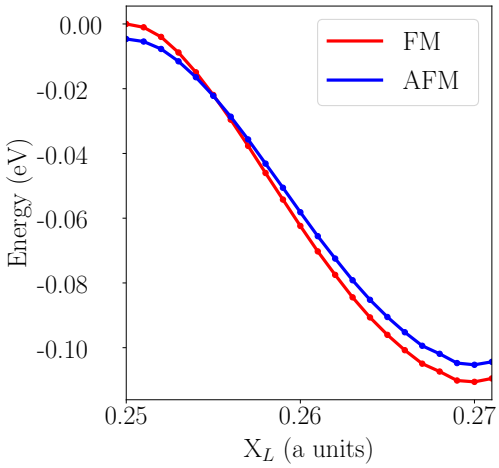

Figure 5.3: Relative energy per formula unit of K_2CuF_4 when it is distorted from the high-symmetry phase I4/mmm (0.25) to the low-symmetry orthorhombic phase. Energies of FM and AFM states at each point have been calculated.

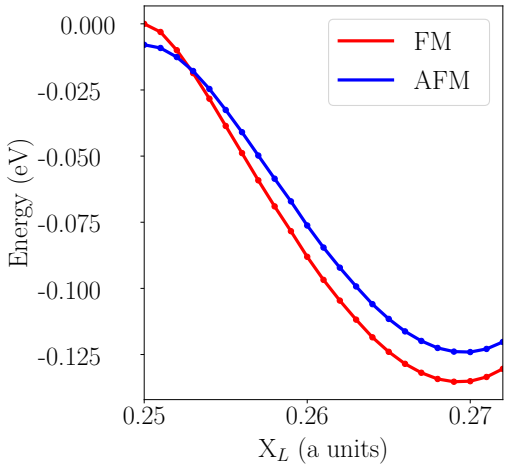

Figure 5.4: Single point relative energy per formula unit of Cs_2AgF_4 at each point of the orthorhombic distortion for FM and AFM configurations.

In high-symmetry phase the ground state of both compounds is AFM, whereas in low-symmetry phase it is FM. Therefore, there is a change in the magnetic order of the ground

state with the orthorhombic distortion. From Figures 5.3 and 5.4 we can see that (1) the energy difference between FM and AFM states, as reflected in Table 5.3 is slightly higher in the low-symmetry phase for both systems, (2) these energy gaps are larger in Cs_2AgF_4 than in K_2CuF_4, (3) the curvature of both magnetic states is greater in K_2CuF_4, which is related with the force constant K of metal-ligand bonds. The force constant is larger for Cu^{2+}-F^- than Ag^{2+}-F^- bonds, which is also reflected in bond distances, which are shorter in the former (see Tables 5.1 and 5.2) and (4) the minimun of Cs_2AgF_4 is $\sim$25 meV deeper than that of K_2CuF_4.

The crossover between FM and AFM states can be understood in terms of a general model based on superexchange and PJT effect, proposed in [44]. This model shows how FM states lead to structural distortions in terms of spin-lattice coupling, considering M-X-M chain with the ligand orbital full and two unpaired electrons in metal orbitals, as usual in Anderson superexchange model. Materials exhibit spin-phonon coupling display a strong dependence of vibrational modes with their magnetic states [44]. As shown in Table 5.4, AFM states lead to softer frequencies than FM, and thus, FM order induces stronger stabilization. The covalent contributions of PJT effect lead to greater values of vibronic contribution to the force constant K^ν in FM sates, and thus, the total force constant $K = K^{(0)} - K^\nu$ is smaller in FM states, as reflected in the curvature of Figures 5.3 and 5.4. On the other hand, the effect of covalence also appears when the composition of the layered system changes from copper compound to silver compound. Indeed, in Cs_2AgF_4, the energy minimum is deeper and the curvature is lower than in K_2CuF_4 as a consequence of the increase in covalence and lattice size.

By contrast to AgF_2, where the difference between the magnetic configurations is $\Delta E =$ 37 meV (Section 4.3), in K_2CuF_2 and Cs_2AgF_4 this difference is smaller, $\Delta E \sim 5 - 10$ meV. It is important to note that the magnetic interaction is not direct but driven by the ligands, precisely, by the equatorial ligands. The distortion modifies the atomic position of equatorial ligands, inducing the change in the magnetic order of the fluoride perovskites. Lattice parameters are kept fixed, whereas in AgF_2 we displaced simultaneously the six ligands of the complexes as well as the cell parameters (see Figure 4.6). In this case, the change in the magnetism is caused by the cooperative distortion of both atomic and cell degrees of freedom.

The same orthorhombic distortion has been applied to La_2CuO_4. Unlike the fluorides, we have found that this system is stable under orthorhombic deformations, with a strong AFM coupling in the equatorial plane. It can be noted a decrease in the energy gap between FM and AFM states as the distortion coordinate increase, which is $\sim 10\%$ of ΔE (see Table 5.3, Figure 5.5).

By means of frequency calculation in the high-symmetry phase of La_2CuO_4 with Crystal code, we have found two unstable vibrational modes of frequencies $\omega = 113i$ cm^{-1} and $\omega = 38i$ cm^{-1} of symmetries B_g and B_u respectively. The first produces the tiltings of CuO_6^{8-} complexes. The last one represents a displacement of the axial ligands O^{2-} and La^{3+} in their **xy** plane. It is a soft mode that is not observed since it leads to less deep minimum. If open shell Cu^{2+} ions are replaced by closed shell Zn^{2+} in low-symmetry phase, the tiltings remain, which suggest that this distortion is not associated with vibronic coupling of an electronic E_g state.

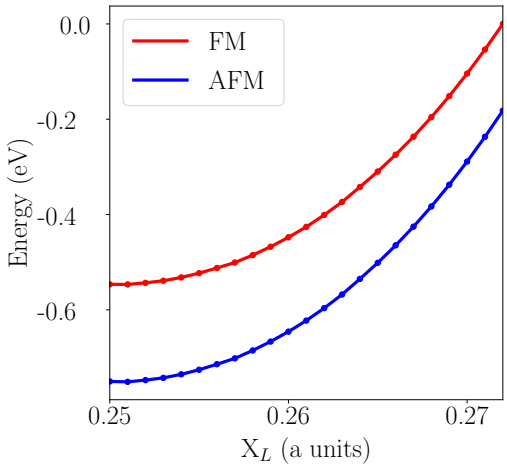

Figure 5.5: Relative energy per formula unit against orthorhombic distortion coordinate in La_2CuO_4 for FM and AFM phases.

5.3. Band structure and density of states

Considering the results shown in Section 5.2, where we have seen that, due to PJT coupling, there is an instability of the high-symmery phases, whose symmetries are reduced from tetragonal to orthorhombic. The fluorides K_2CuF_4 and Cs_2AgF_4 are distorted following a vibrational mode that displaces the equatorial ligands F^-, leading the systems to an adiabatic minimum. The displacement of fluorine ions is accompanied by a change in the magnetic order from AFM in the parent phase to FM in the low-symmetry phase. Therefore, our model has been built involving the transition-metal ion and the ligands.

This model assumes that the interaction between layers is negligible and thus, the dispersion of the bands should be also negligible along the axial direction. Then, from first-principles simulations we have obtain the band diagram for path $\Gamma \to X \to M \to \Gamma \to Z$, where we can see that the bands in $\Gamma \to Z$ path are essentially flat (see slight red bands (FP) depicted in Figures 5.6 and 5.7).

In a first step, we have obtain the band structure from first- and second-principles for K_2CuF_4 represented in Figures 5.6 (high-symmetry phase, HS) and 5.7 (low-symmetry phase, LS). As indicated in these figures, the band diagrams for both FM and AFM states have been calculated. It can be noted that this system has the least covalent character among the three layered perovskites and its orbitals are most localized, so, in principle, the model should better fit this compound. The modelization of Cs_2AgF_4 and La_2CuO_4 is now in progress, since their parametrizations require further analysis.

As explained in Section 2.4, the model has seven parameters, whose values for K_2CuF_4 system are gathered in Table 5.5. These parameters are the self-terms of each involved orbital γ_{ab}, the metal-ligand interaction V_{pd}^{RAG}, its variation with the distance $V'_{pd} = \vec{f}\delta\vec{r}_{a,b}$, which controls the change from high-symmetry to low-symmetry, and the screened on-site Coulomb term U and exchange interaction J.

$\gamma_{3z^2-r^2}$ (eV)	$\gamma_{x^2-y^2}$ (eV)	γ_{p_σ} (eV)	V_{pd}^{RAG} (eV)	V'_{pd} (eV)	U (eV)	J (eV)
-1.489	-4.689	-2.889	-1.3	9.0	7.5	1.0

Table 5.5: Parameters used to calculate the bands of K_2CuF_4 from our second-principles model. Their values have been obtained by fitting the bands from first-principles calculations.

The parameters collected in Table 5.5 provide the second-principles bands represented in Figures 5.6 and 5.7. As explained in Section 2.4, we have used a simple model, which is a first approximation to the problem and whose parameters will be refined in future works. Nevertheless, it is worth noting that, from this model, we have been able to reproduce the magnetic order obtained from first-principles simulations for the ground state of both high-symmetry and low-symmetry phases of K_2CuF_4. The energy differences between the two magnetic configurations are as follows: $\Delta E_{\mathrm{HS}} = 8.3$ meV and $\Delta E_{\mathrm{LS}} = 2.6$ meV. These results are rather similar to those obtained from first-principles calculations (see Table 5.3).

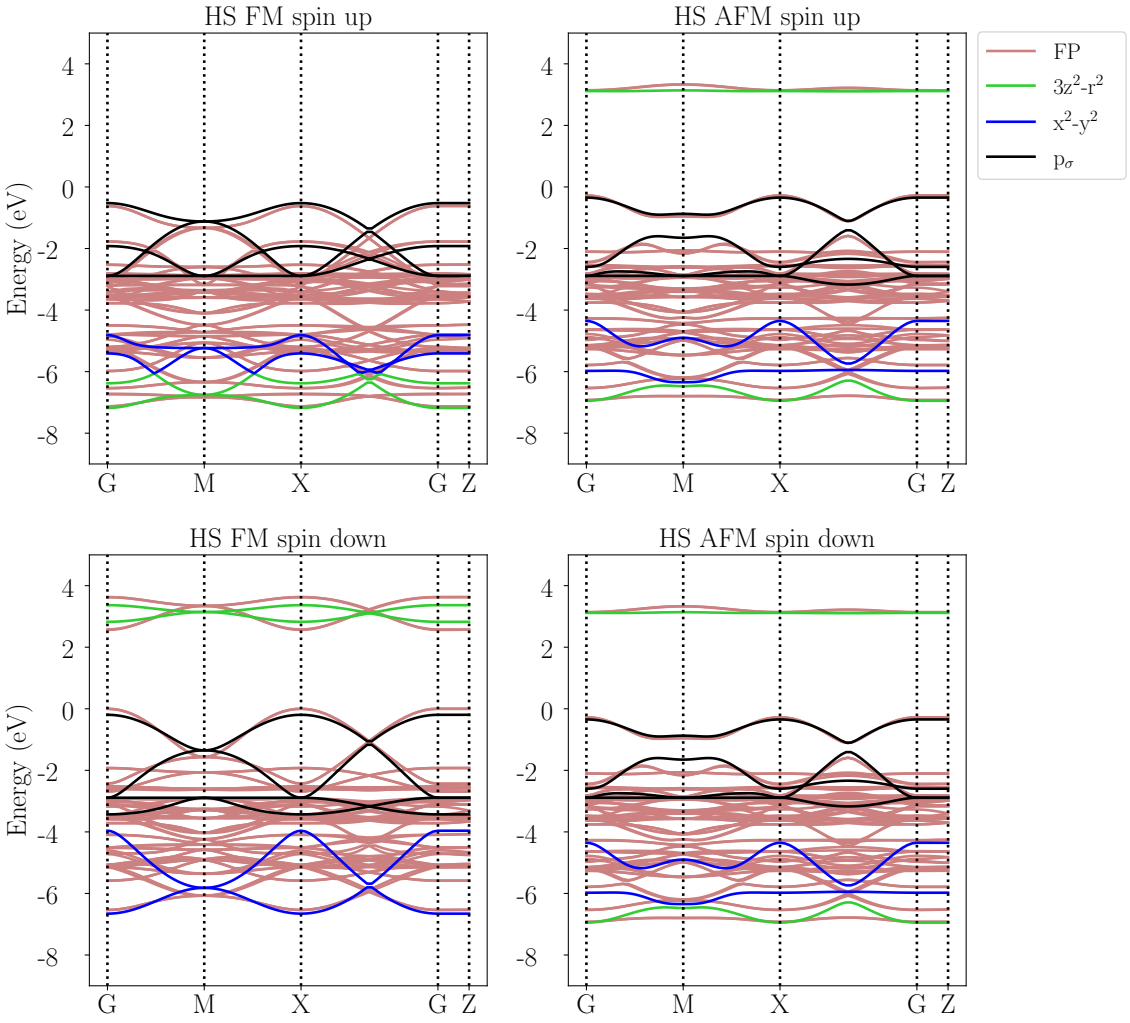

Figure 5.6: Band diagram by spin channel of high-symmetry I4/mmm phase (HS) of K_2CuF_4. The magnetic order (FM or AFM) and the spin channel (up or down) are indicated in the title of each panel. The bands obtained from first-principles calculations (FP) are represented in slight red, while the character of the bands calculated by our second-principles model ($3z^2 - r^2$ in green, $x^2 - y^2$ in blue and p orbitals of ligands in black) is indicated in the legend.

From first-principles band calculation we have observed a splitting between the spin up and spin down bands of AFM state in the low-symmetry compound, which is vanished when the symmetry is that of the parent phase. This splitting is due to the orthorhombic symmetry of the complexes, which implies an asymmetric spin distribution in certain directions. This effect, which has been observed in Cs_2AgF_4 too, is the basis of AFM spintronics. Spintronics are usually based on FM materials, where the spin-polarization is induced to strongly couple with the global magnetization. On the other hand, AFM requires a

local non-equilibrium spin-polarization with alternated sign between lattice sites. This is achieved combining broken spatial inversion symmetry and spin-orbit coupling, which leads to a current-induced spin-polarization [45].

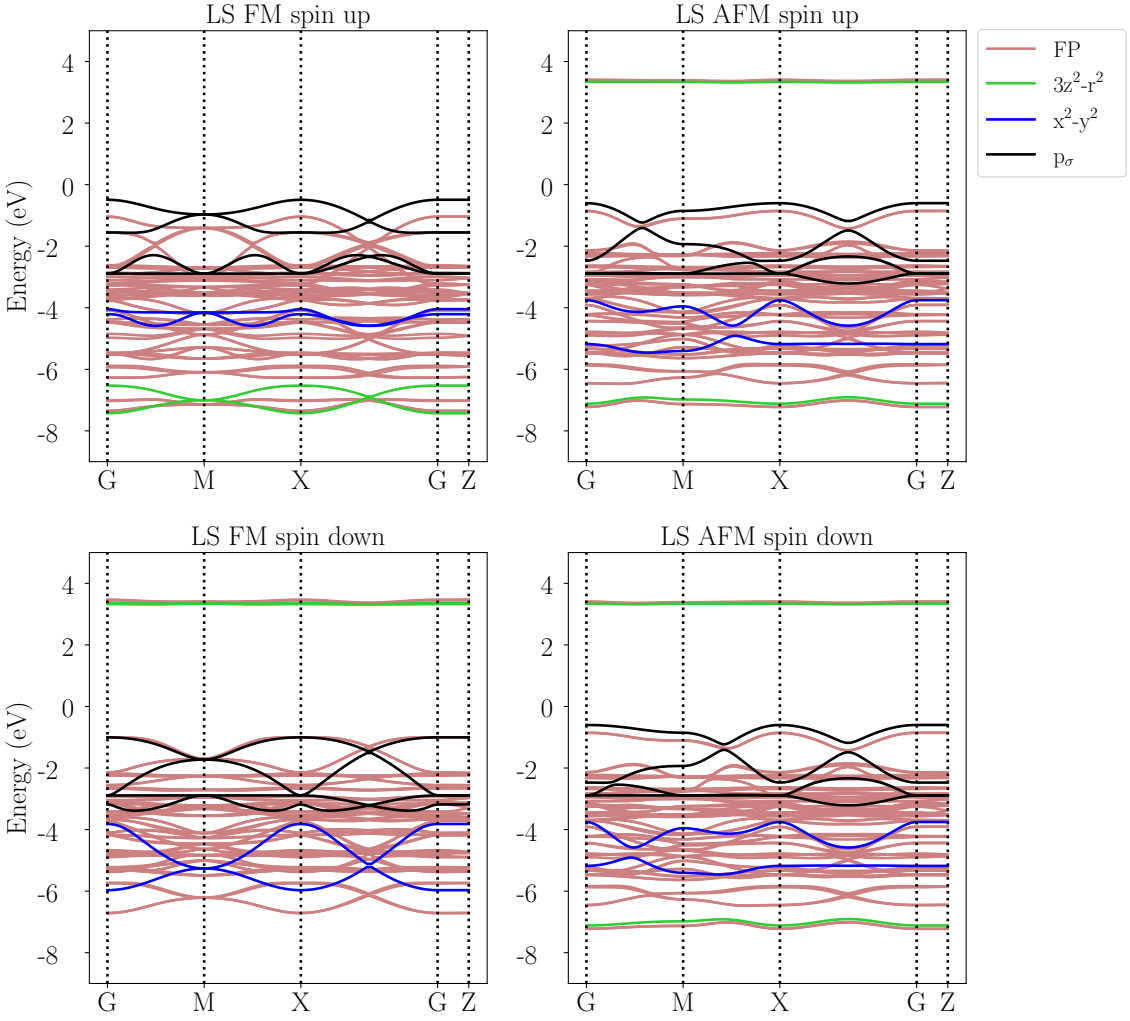

Figure 5.7: Band diagram by spin channel of low-symmetry Cmca phase of K_2CuF_4. The magnetic order (FM or AFM) and the spin (up or down) are indicated above each panel. Slight red bands are the results of first-principles calculations (FP) and green, blue and black bands are the ones obtained from second-principles, whose character is indicated in the legend.

In order to explore the character of the bands represented in Figure 5.6, we have calculated the projected density of states of the high-symmetry phase for both FM and AFM states. This PDOS is represented in Figure 5.8.

From the PDOS we have seen that, as expected from tetragonal symmetry, p_x and p_y orbitals of the two equatorial ligands and xz and yz orbitals of the central metal cation are degenerated. Furthermore, the hole is localized in $3z^2 - r^2$ orbital. Therefore, we can clearly identify the bands corresponding to this orbital in the band diagram, as indicated.

On the other hand, we have assumed that the bands associated with the p ligand orbitals are those corresponding to the states closest to the Fermi level, which are quite dispersive, and those corresponding to $x^2 - y^2$ orbital are in the range from -6 to -4 eV, at the bottom of the diagram. Therefore, from the PDOS, a first approximation of the values of $\gamma_{3z^2-r^2}$,

$\gamma_{x^2-y^2}$ and γ_{p_σ} can be extracted. On the other hand, the spliting between $3z^2-r^2$ bonding and antibonding orbitals can be related with the screened Coulomb parameter. The value provided by first-principles is ~ 9.5 eV, which has been refined in order to obtain a better fit of the bands. Both Coulomb U and exchange J parameters are similar to those found by Liechtenstein et al. in $KCuF_3$ ($U = 7.5$ eV, $J = 0.9$ eV) [46].

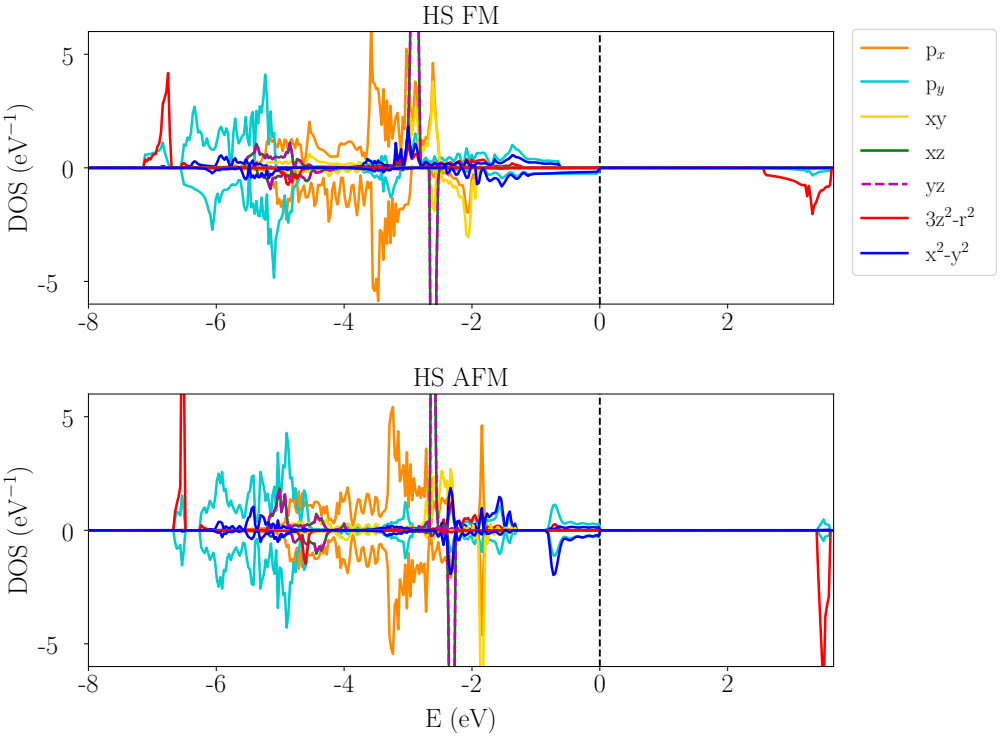

Figure 5.8: Projected density of states of high-symmetry phase of K_2CuF_4 for both FM and AFM orders. The density of states has been projected over the basis functions of d orbitals of Cu^{2+} and p_x and p_y orbitals of two F^- (two equatorial ligands).

Considering the high-symmetry band diagram and PDOS, one can see that the band corresponding to $3z^2 - r^2$ in FM state is more dispersive than for the AFM state, as correspond to parallel spins. On the other hand, $3z^2 - r^2$ band are flatter than $x^2 - y^2$ or ligand bands, since the interaction in the **ab** plane is larger.

Finally, it should be mentioned that, since it is a very basic model, one can see discrepancies between first- and second-principles bands. Regarding high-symmetry (HS) bands (Figure 5.6), for the FM state in spin up channel, the shape of the bands is quite similar to first-principles and the large differences are found in point M and in $X \to \Gamma$ path. However, in the spin down channel, for $x^2 - y^2$ and p bands the dispersion is greater than in first-principles. In the AFM case, we can observe a shift in bonding $3z^2 - r^2$ as well as in $x^2 - y^2$ bands. Considering ligand bands, the largest difference is also found in point M of reciprocal space.

As can be seen in Figure 5.7, the difference between first- and second-principles bands increases when the symmetry is reduced from tetragonal I4/mmm to orthorhombic Cmca. It can be observed that the shape of ligand bands is quite similar but there is a general shift from first-principles bands. Since the distortion occurs in the equatorial plane, the greatest differences are found in $x^2 - y^2$ band, whereas $3z^2 - r^2$ is well represented. It is worth noting that the low-symmetry bands are controlled by just one parameter, V'_{pd}, which difficult the fit of the bands.

5.4. Ferroelasticity

As explained in Section 1.3 and 5.2, lattice distortions play and important role on physical properties such as magnetism or orbital ordering of layered perovskites. Along this line, in the last part of this work we have been focused on controlling the magnetic order through the variation of cell paramenters. The control of magnetism by means of distortion-induced strains has significant consequences since, experimentally, the lattice response of a thin film can be modified by the epitaxial growth on certain substrates [47].

If lattice parameters $\vec{a}$ and $\vec{b}$ (equatorial plane) are compressed, the ions get closer to each other so the number of interactions increases. The overlap among electron clouds is higher and, therefore, electronic repulsion is larger. On the other hand, the attractive forces also increase so, in general, the bonds become stronger. Under these conditions, the primary force constant $K^{(0)}$ should be greater and thus, the instability would be weakened and the minimun would be less deep. Regarding the magnetic order, the splitting between electronic states will be larger, favoring AFM configuration.

The energy against the orthorhombic distortion in K_2CuF_4 and Cs_2AgF_4 when lattice parameters are compressed by 5% (left) and 7% (right) of their values is represented in Figures 5.9 and 5.10.

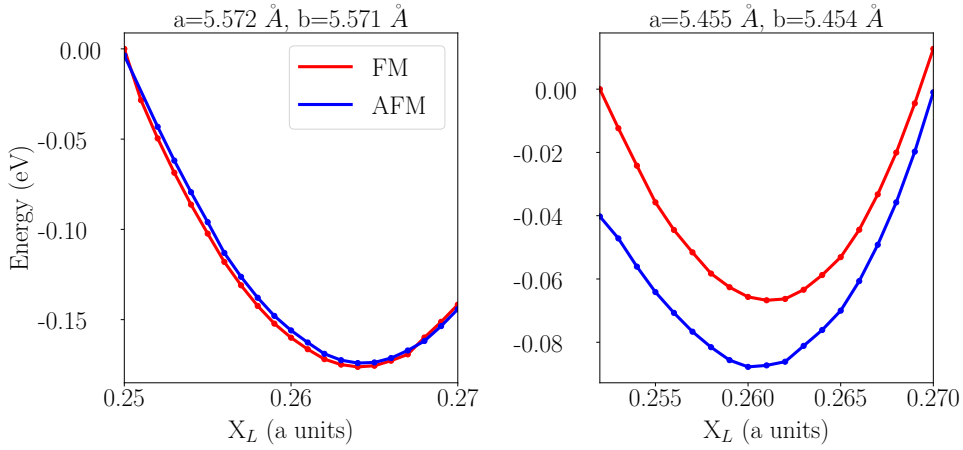

Figure 5.9: Relative energy per formula unit of K_2CuF_4 when it is distorted from high-symmetry phase to low-symmetry phase for both FM and AFM orders. Energies have been obtained compressing lattice parameters $\vec{a}$ and $\vec{b}$ by 5% (left) and 7% (right) and optimizing $\vec{c}$.

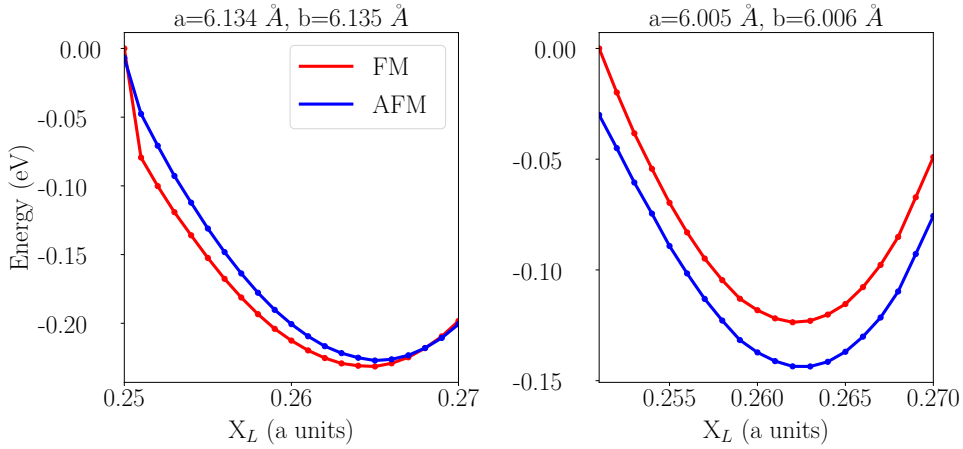

Figure 5.10: Energy gained with orthorhombic distortion in Cs_2AgF_4 for FM and AFM states. Cell parameters $\vec{a}$ and $\vec{b}$ have been compressed by 5% (left) and 7% (right) and $\vec{c}$ was optimized.

In Figures 5.9 and 5.10 we can see that a compression of 5% is not enough to stabilize the AFM state in low-symmetry phase. By contrast, if lattice parameters $\vec{a}$ and $\vec{b}$ are compressed by 7%, the AFM state is lower in energy than the FM state, with an energy difference of ∼21 meV in both K_2CuF_4 and Cs_2AgF_4.

Contrary to expectations, in K_2CuF_4 and Cs_2AgF_4 we can observed that the energy gained with the orthorhombic distortion is higher when lattice parameters are compressed by 5%, if we compared these results with the ones represented in Figures 5.3 and 5.4, so the instability is enhanced. This can be briefly discuss within a simplified PJT model.

In high-symmetry configuration, where the electron density of complexes is symmetric, the overlap between metal and ligand orbitals is zero since their mixing is forbidden by symmetry. When the open shell ion Cu^{2+} is introduced, forming a CuF_6^{4-} complex, there is an orthorhombic vibrational mode $Q_{b_{1g}}$, belonging to irrep B_{1g}, that couples states separated by an energy gap, producing the orthorhombic distortion displayed in Figure 5.2. Within this model, metal and ligands orbitals are the ones represented in Figure 5.11

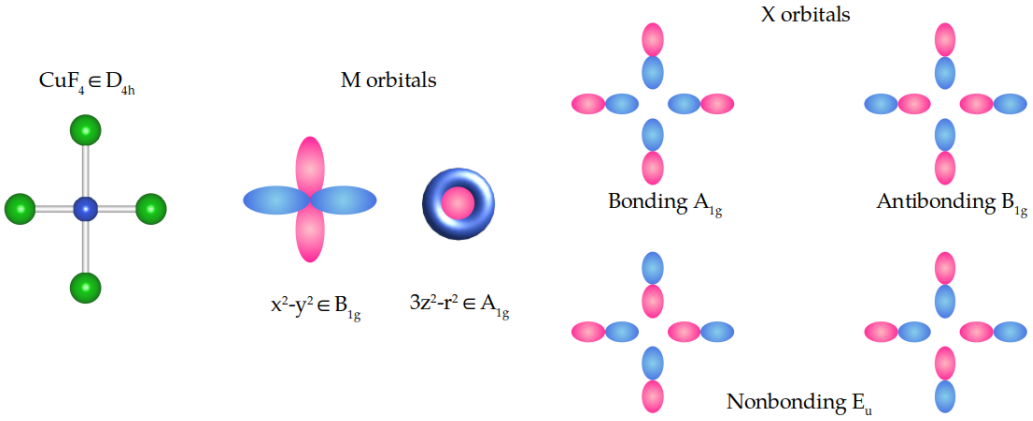

Figure 5.11: Metal and ligand orbitals in tetragonal D_{4h} symmetry within a simple model of MX_4 complex in **ab** plane. The irrep of each orbital is indicated in the sketch.

The vibrational mode $Q_{b_{1g}}$ produces the mixing of metal and ligands electronic states and thus, the overlap is not zero. Assuming that $\phi_{3z^2-r^2}$ and $\phi_{x^2-y^2}$ are the wave functions associated with the central cation and $\phi_{L,B_{1g}}$ and $\phi_{L,A_{1g}}$ the wave function associated with the bonding and antibonding σ orbitals of the ligands, there are two contributions to the vibronic constant K^ν (Equation 3.17)

$$K_1^\nu = \frac{|\langle\phi_{3z^2-r^2}|Q_{b_{1g}}|\phi_{L,B_{1g}}\rangle|^2}{E(\phi_{3z^2-r^2}) - E(\phi_{L,B_{1g}})} \tag{5.3}$$

$$K_2^\nu = \frac{|\langle\phi_{x^2-y^2}|Q_{b_{1g}}|\phi_{L,A_{1g}}\rangle|^2}{E(\phi_{x^2-y^2}) - E(\phi_{L,A_{1g}})} \tag{5.4}$$

where the direct product $B_{1g} \otimes B_{1g} \in A_{1g}$, and therefore $K_1^\nu \neq 0$ and $K_2^\nu \neq 0$. As explained in Section 3.3, the vibronic constant depends on both the intensity of the vibronic coupling and the energy difference between the electronic states. In this case, we have two couplings which will be influenced by the strain when lattice parameters are compressed. It should be noted that, although the main contribution comes from K_2^ν, the vibronic coupling between $\phi_{3z^2-r^2}$ and $\phi_{L,B_{1g}}$ is more affected by the strain, since the overlap between these orbitals is lower than that between $\phi_{x^2-y^2}$ and $\phi_{L,A_{1g}}$. Thus, the former will change significantly

with the strain, which will be accompanied by a variation of the energy as well as of the charge distribution of molecular orbitals.

On the other hand, in La_2CuO_4, the hole is localized in $x^2 - y^2$ orbital, whose overlap with p orbitals of the ligands is greater than that of $3z^2 - r^2$. Hence, the impact of strains induced by lattice distortions will be, in principle, less significant in this system.

6. Final remarks

In this work we have shown, by means of computational simulations, that the crystalline and magnetic structures of silver difluoride AgF_2 and layered perovskites K_2CuF_4, Cs_2AgF_4 and La_2CuO_4 are correlated. In AgF_2, the magnetic order is a direct consequence of cooperative JT effect. By contrast to the three other systems, its parent phase is cubic and thus, devoid of any layering. Furthermore, as reflected in the band structure, the JT effect produced in this lattice cannot destroy the inter-layer band dispersion. In the case of layered perovskites, the origin of their structure is found in the composition, where MX_2 planes are separated by rock salt AX planes, which almost prevents inter-layer interaction.

On the other hand, it can be noted that the change in the magnetism of K_2CuF_4 and Cs_2AgF_4 comes from the variations in the electron density due to PJT effect, which affect the covalency of these systems and lead to stronger stabilization in FM states. The stabilization is greater in the silver compound since covalency effects are more significant and, additionally, lattice size is larger than in K_2CuF_4. These two systems, like AgF_2, display ferroelasticity, where the strains produced by distortions control the magnetic coupling. The next step in K_2CuF_4 and Cs_2AgF_4 is quantifying the change in molecular orbitals energy and charge distribution with the strains, which will be included in future works.

However, as mentioned above, the origin of distortions in silver difluoride and layered perovskites is different. As shown in previous sections, the ground state of the parent $Pa\bar{3}$ phase of AgF_2 belongs to the trigonal type of symmetry D_{3d}, displaying a true E_g degeneracy, which gives rise to distortions whose origin lies in JT effect. On the other hand, the parent phase of layered perovskites is tetragonal I4/mmm, devoid of degeneration, which prevents the existence of JT effect. At this point, it should be stressed the importance of symmetry in the analysis of vibronic coupling problems, since the microscopic origin of structural instabilities can be understood in terms of the symmetry of the parent phases, which is key to predict and study properties of materials.

The design of new systems requires thorough analysis of structure and properties of current materials. Nevertheless, understanding the effects present in this sort of materials is complicated since there are many distortions, interactions and defects (vacancies, impurities, dislocations and so on) producing complex states, whose modelling can be problematic. Along this line, first- and second-principles simulations as well as model hamiltonian methods will be combined to study the interaction and competition among structural, orbital and spin orderings. In that direction, second-principles models for Cs_2AgF_4 and La_2CuO_4 are now in development.

References

[1] J.B. Bednorz, K. Müller, Possible high-T_C superconductivity in the Ba-La-Cu-O system, Z. Phys. B Condens. Matter **1986**, 64, 189–193.

[2] Y. Kamihara, T. Watanabe, M. Hirano, H. Hosono, Iron-Based Layered Superconductor La[$O_{1-x}F_x$]FeAs (x = 0.05-0.12) with T_C = 26 K, J. Am. Chem. Soc. **2008**, 130, 3296–3297.

[3] H. Y. Hwang, Y. Iwasa, M. Kawasaki, B. Keimer, N. Nagaosa, Y. Tokura, Emergent phenomena at oxide interfaces, Nat. Mater. **2012**, 11, 103-113.

[4] W. Grochala, Silverland: the realm of compounds of divalent silver – and why they are interesting, J. Supercond. Nov. Magn. **2018**, 31, 737-752.

[5] W. Grochala, Small changes, big consequences, Nat. Mat. **2006**, 5, 512-514.

[6] S.E. McLain, M.R. Dolgos, D.A. Tennant, J.F.C. Turner, T. Barnes, T. Proffen, B. C. Sales, R.I. Bewley, Magnetic behaviour of layered Ag(II) fluorides, Nat. Mat. **2006**, 5, 561-566.

[7] J. Tong, R.K. Kremer, J. Köhler, A. Simon, C. Lee, E. Kan, M. Whangbo, The layered ferromagnet Cs_2AgF_4: antiferromagnetic inter-layer coupling driven by magnetic dipole-dipole interactions, Z. Kristallogr. **2010**, 225, 498-503.

[8] Y. Krockenberger, B. Eleazer, H. Irie, H. Yamamoto, Superconducting- and Insulating-Ground States in La_2CuO_4 Structural Isomers, J. Phys. Soc. **2014**, 83, 114602.

[9] D.V. Fil, O.I. Tokar, A.L. Shelankov, W. Weber, Lattice-mediated interaction Cu^{2+} Jahn-Teller ions in insulating cuprates, Phys. Rev. B **1992**, 45, 5633-5640.

[10] M.K. Shen, J.C. Seamus, Cuprate high-T_C superconductors, Materials Today **2008**, 11, 9, 14-21.

[11] Z. Mazej, D. Kurzydlowski, W. Grochala, Unique Silver (II) Fluorides: The Emerging Electronic and Magnetic Materials. In Photonic and Electronic Properties of Fluoride Materials **2016**, Elsevier, 231-260.

[12] A. Grzelak, S. Haibin, X. Yang, D. Kurzydlowski, J. Lorenzana, W. Grochala, Epitaxial engineering of flat silver fluoride cuprate analogs, Phys. Rev. Materials **2020**, 4, 084405.

[13] P. Fischer, D. Schwarzenbach, H.M. Rietveld, Crystal and magnetic structure of silver difluoride: I. Determination of the AgF_2 structure, J. Phys. Chem. Solids **1971**, 32, 543-550.

[14] X. Xu, Y. Ma, T. Zhang, C. Lei, B. Huang, Y. Dai, Prediction of two-dimensional antiferromagnetic ferroelasticity in AgF_2 monolayer, Nanoscale Horizons **2020**, 5, 1386-1393.

[15] R. J. Tilley, Perovskites: Structure-Properties Relationships, Wiley, Chichester, **2016**.

[16] C. B. Mitzi, Introduction: Perovskites, Chem. Rev. **2019**, 119, 3033-3035.

[17] A. Piegari, F. Flory, Optical thin films and Coatings, Woodhead Publishing (second edition), Cambridge **2018**.

[18] X. Kuang, K. Zhou, Study of exchange interaction of Ni^{2+} pairs in MgO: Ni^{2+}, $KMgF_3$: Ni^{2+} and $KNiF_3$ crystals, Physica B: Condensed Matter **2001**, 305, 2, 169-174.

[19] P. García-Fernández, M. Moreno, J.A. Aramburu, Electrostatic control of orbital ordering in noncubic crystals, Phys. Chem. C **2014**, 118, 7554-7561.

[20] J. Kanamori, Crystal distortion in magnetic compounds, J. Appl. Phys. **1960**, 31, S14-S23.

[21] K.I. Kugel, D.I. Khomskii, The Jahn-Teller effect and magnetism: transition metal compounds, Sov. Phys., Usp. **1982**, 25(4).

[22] M.V. Mostovoy, D.I. Khomskii, Orbital ordering in charge transfer insulators, Phys. Rev. Lett. **2004**, 92, 167201.

[23] R. M. Martin, Electronic Structure: Basic Theory and Practical Methods, Cambridge University Press, Cambridge, **2004**.

[24] F. Jensen, Introduction to Computational Chemistry, Ed. Wiley, Odense, **2008**.

[25] A. Jakobsson, Ab initio Studies on Exchange Interactions in Metals and Correlated Oxides, Uppsala Universitet, Uppsala, **2016**.

[26] R. Dovesi et al, CRYSTAL17 User's Manual, University of Torino, Torino, **2017**.

[27] CRYSTAL basis sets https://www.crystal.unito.it/basis-sets.php (accesesed on March 2021)

[28] G. te Velde et al, Chemistry with ADF, J. of Comp. Chem. **2001**, 22, 931.

[29] P. García-Fernández, J.C. Wojdel, J. Íñiguez, J. Junquera, Second-principles method for materials simulations including electron and lattice degrees of freedom, Phys. Rev. B. **2016**, 93, 195137.

[30] J.S. Griffith, The Theory of Transition-Metal Ions, Cambridge University Press, Cambridge, **1961**.

[31] V. I. Anisirnov, O. Gunnarsson, Density-functional calculation of effective Coulomb interactions in metals, Phys. Rev. B **1991**, 43, 7570-7574.

[32] I.B. Bersuker, The Jahn-Teller Effect, Cambridge University Press, Cambridge, **2006**.

[33] J.M. García-Lastra, M.T. Barriuso, J.A. Aramburu, M.Moreno, Forces due to changes of electronic density: A complementary view of the Jahn–Teller effect, Chem. Phys. **2005**, 317, 103-110.

[34] T. A. Abtew, Y. Y. Sun, B. Shih, P. Dev, S. B. Zhang and P. Zhang, Dynamic Jahn-Teller Effect in the NV^- Center in Diamond, Phys. Rev. Let. **2011**, 107, 146403.

[35] P. García-Fernández, I.B. Bersuker, J.A. Aramburu, M. Barriuso, M. Moreno, Origin of warping in the E⊗e Jahn-Teller problem: Quadratic vibronic coupling versus anharmonicity and application to NaCl: Rh^{2+} and triangular molecules, Phys. Rev. B. **2005**, 71.

[36] P. García-Fernández, A. Trueba, M.T. Barriuso, J.A. Aramburu, M. Moreno, Dynamic and Static Jahn-Teller Effect in Impurities: Determination of the Tunneling Splitting, Prog. Theor. Chem. Phys. **2011**, 23, 105-142.

[37] I.B. Bersuker, Modern aspects of the Jahn-Teller effect theory and applications to molecular problems, Chem. Rev. **2001**, 101, 1067-1114.

[38] R.D. Shannon, C.T. Prewitt, Effective ionic radii in oxides and fluorides, Acta Crystallogr. B **1969**, 25, 925

[39] M.A. Augustyniak-Jablokow, Y.V. Yablokov, K. Lukaszewicz, A. Pietraszko, V.E. Petrashen, V.A. Ulanov, Continuous changes of the Jahn–Teller deformation of $Cu(H_2O)_6$ complex in ferroelastic $Cs_2Cu(ZrF_6)_2{\cdot}6H_2O$ crystal, Chem. Phys. Lett. **2001**, 344, 345-351.

[40] J. Vannimenus, G. Toulouse, Theory of the frustration effect. II. Ising spins on a square lattice, J. Phys. C: Solid State Phys. **1977**, 10.

[41] P. Fischer, G. Roult, D. Schwarzenbach, Crystal and Magnetic Structure of Silver Difluoride II. J. Phys. Chem. Solids **1971**, 32, 1641-1647.

[42] M. Hidaka, K. Inoue, I. Yamada, P.J. Walker, X-ray diffraction study of the crystal structures of K_2CuF_4 and $K_2Cu_xZn_{1-x}F_4$, Physica B, C **1983** 121, 343-350.

[43] R. Hord, G. Cordier, K. Hoffmann, A. Buckow, G. Pascua, H. Luetkens, L. Alff, B. Albert, Enhanced two-dimensional behavior of metastable T'-La_2CuO_4, the parent compound of electron-doped cuprate superconductors, Phys. Rev. B **2010** 82, 180508.

[44] P. García-Fernández, J.A. Aramburu, M. Moreno, Influence of magnetic ordering on structural instabilities in insulating perovskites, Phys. Rev. B **2011**, 83, 174406.

[45] T. Jungwirth, J. Sinova, A. Manchon, X. Marti, J. Wunderlich and C. Felser, The multiple directions of antiferromagnetic spintronics, Nat. Phys. **2018**, 14, 200–203.

[46] A.I. Liechtenstein, V.I. Anisimov, J.Zaanen, Density-functional theory and strong interactions: Orbital ordering in Mott-Hubbard insulators, Phys. Rev. B **1995**, 52, 5467-5470.

[47] G. Koster, M. Huijben and G. Rijnders. Epitaxial Growth of Complex Metal Oxides, WP, Cambridge, **2015**.